THERMAL MODELING OF A MECHANICAL INTEGRITY TEST ON AN UNDERGROUND STORAGE CAVERN

by

Brandon C. Lampe

B.S., South Dakota School of Mines and Technology, 2009

A thesis submitted to the

Faculty of the Graduate School of the

University of Colorado in partial fulfillment

of the requirement for the degree of

Master of Science

Department of Civil and Environmental Engineering

2011

This thesis entitled:

Thermal Modeling of a Mechanical Integrity Test on an Underground Storage Cavern
written by Brandon C. Lampe
has been approved by the Department of Civil, Environmental, and Architectural Engineering

_____

Professor John S. McCartney, Ph.D. (committee chair)

_____

Professor Richard A. Regueiro, Ph.D.

_____

Joe L. Ratigan, Ph.D.

Date_____

The final copy of this thesis has been examined by the signatories, and we
Find that both the content and the form meet the acceptable presentation standards
Of scholarly work in the above mentioned discipline.

Lampe, Brandon C. (M.S., Department of Civil, Environmental, and Architectural Engineering)

Thermal Modeling of a Mechanical Integrity Test on an Underground Storage Cavern

Thesis directed by Associate Professor John S. McCartney

ABSTRACT

The objective of this research was to describe how the transient heat transfer phenomena influences the results of mechanical integrity tests (MITs) performed on the well of an underground storage cavern in rock salt. Underground caverns have been developed in salt deposits throughout the world for the purpose of producing brine and storing compressed air, hydrocarbons, and waste products; and are a critical underground infrastructure. Despite the very low permeability of rock salt, limited volumes of stored product may diffuse out of the cavern. Additionally, underground storage caverns change in size because of salt creep, leading to difficulties in estimating the volume of product retained in the cavern. The great importance of these issues create the need to accurately determine if a cavern well has mechanical integrity and therefore suitable for storage. Although MITs on cavern wells are mandated by both federal and state governments, a rigorous standardization of testing procedures has not been developed. Finite element analyses and other numerical methods have been employed to show how local thermal conditions and test duration influence the results of a typical MIT performed on standard well sizes, and how the loss of integrity may be masked by the testing conditions.

ACKNOWLEDGEMENTS

I would like to thank Joe Ratigan for introducing me to this field of research and for his patience, guidance, and intuition.

Additionally, I would like to express my sincere gratitude towards Parsons Brinckerhoff Energy Storage Services, Inc. (PBESS) for their continued employment throughout my education.

Table of Contents

Table of Tables

Table of Figures

1 Introduction

Underground caverns have been developed in rock salt strata throughout the world for the purpose of producing brine and storing compressed air, hydrocarbons, and waste products. The low incident (e.g. a reportable leak from or failure of a storage cavern) occurrence rate associated with storage in rock salt along with low ratios of surface area, construction cost, and maintenance cost to storage volume when compared with alternative means of storage results in rock salt being a favored storage medium [Evans, 2008]. Also, intact rock salt has a very low value of intrinsic permeability (10^{-19} to 10^{-22} m^2), which is largely because of its "self-healing" property [Djahanguiri and Matthews, 1983]. Despite the low permeability of rock salt, limited volumes of stored products may diffuse into the salt surrounding the cavern. Additionally, underground storage caverns change in size because of salt creep, leading to difficulties in estimating the volume of product stored in the cavern [e.g. Van Sambeek et al., 2005; Bérest et al., 2001]. The great importance of these issues result in the need to accurately determine if a cavern well has mechanical integrity and therefore suitable for storage; the goal of this research is to provide insight towards how this may be achieved.

A storage cavern is connected to the ground surface via a cased and cemented well that typically penetrates through stratigraphic layers that are more permeable than salt. Although very limited product diffusion from the cavern into the surrounding salt formation may potentially occur through the rock-salt matrix, most researchers agree the likely path for leakage to occur from the storage system (i.e. the cavern and associated well) is through the cemented casing and/or at the casing shoe (bottom of lowermost cemented casing) and therefore tests have been developed to analyze these regions [e.g. Van Sambeek et al., 2005; Nelson and Van Sambeek, 2003; Bérest et al., 2001]. The ability of a storage system (Figure 1) to prevent leakage of the stored product into the surrounding environment is termed external integrity or tightness [Crotogino, 1995]. The desired degree of tightness, which has no absolute value, of a storage system is dependent on the economic nature of the stored product and the sensitivity of the local biological, geological, and hydrogeological environments to the product, as well as the regulatory environment. An evaluation of tightness is typically required in most countries upon the commissioning of a storage system and at five year intervals thereafter through a procedure known as a mechanical integrity test (MIT) [e.g. Gatelier et al., 2008; KDHE, 2005; Nelson and Van Sambeek, 2003; Van Sambeek et al., 2005]. Although there are several different types of

MITs that vary with procedure and testing materials, this research is focused specifically on the Nitrogen/Brine Interface Test (NBT), which is a common testing method especially for large storage systems typical of the United States Gulf Coast region.

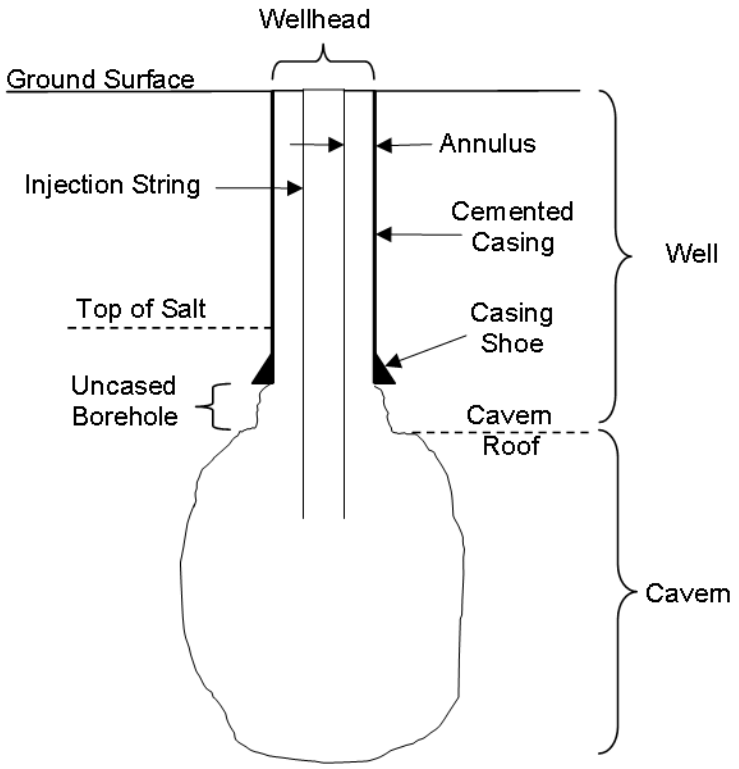

Figure 1 Generalized description of a storage system (not to scale).

Although the NBT is commonly implemented to assess the integrity of a storage system, there are very few guidelines outside the state of Kansas [KDHE, 2005] currently in place for regulating the duration of time between sequenced events that are performed during the test. The specific objective of this research is to better understand how and to what extent the variation of time between particular events during a NBT, the well geometry, and the surface temperature during the NBT may influence test results; this has been accomplished through numerical modeling of the heat transfer phenomena associated with the NBT on an array of idealized storage-well geometries with differing surface temperatures and the calculation of theoretical test results.

2 Background of NBT

Nitrogen gas is a common test fluid used in a MIT because it is inert and readily available in most locations; its physical properties have also been well studied and documented. The low viscosity of nitrogen gas allows it to leak through a fracture at a rate 2 to 50 times that of other commonly stored fluids (typically hydrocarbons); and therefore MITs performed with nitrogen gas result in a higher degree of sensitivity than would be possible with other typical testing fluids [Heitmann, 1987].

Determining the integrity of an underground storage system in salt essentially involves calculating the apparent leak rate from the storage system. The apparent leak rate is the calculated leak rate from the storage system to the external environment, which may vary considerably from the actual leak rate, depending on the manner in which the test is executed and analyzed. The apparent leak rate is calculated during a NBT by determining the change of nitrogen mass/volume stored in the cased annular (between the injection string and cemented casing) and uncased borehole regions over the duration of the test.

2.1 Generalized Description of the Nitrogen/Brine Interface Test (NBT)

During a typical NBT, two specific regions of a well are tested (Figure 2) by monitoring the wellhead pressure, injection string temperature, and nitrogen/brine interface depth (determined via a logging tool run on a wireline in the injection string) over a measureable time period; the two specific test areas are: (A) the cemented casing from the casing shoe up to the ground surface and (B) the casing shoe and uncased borehole region below the casing shoe and above the cavern roof up to the ground surface.

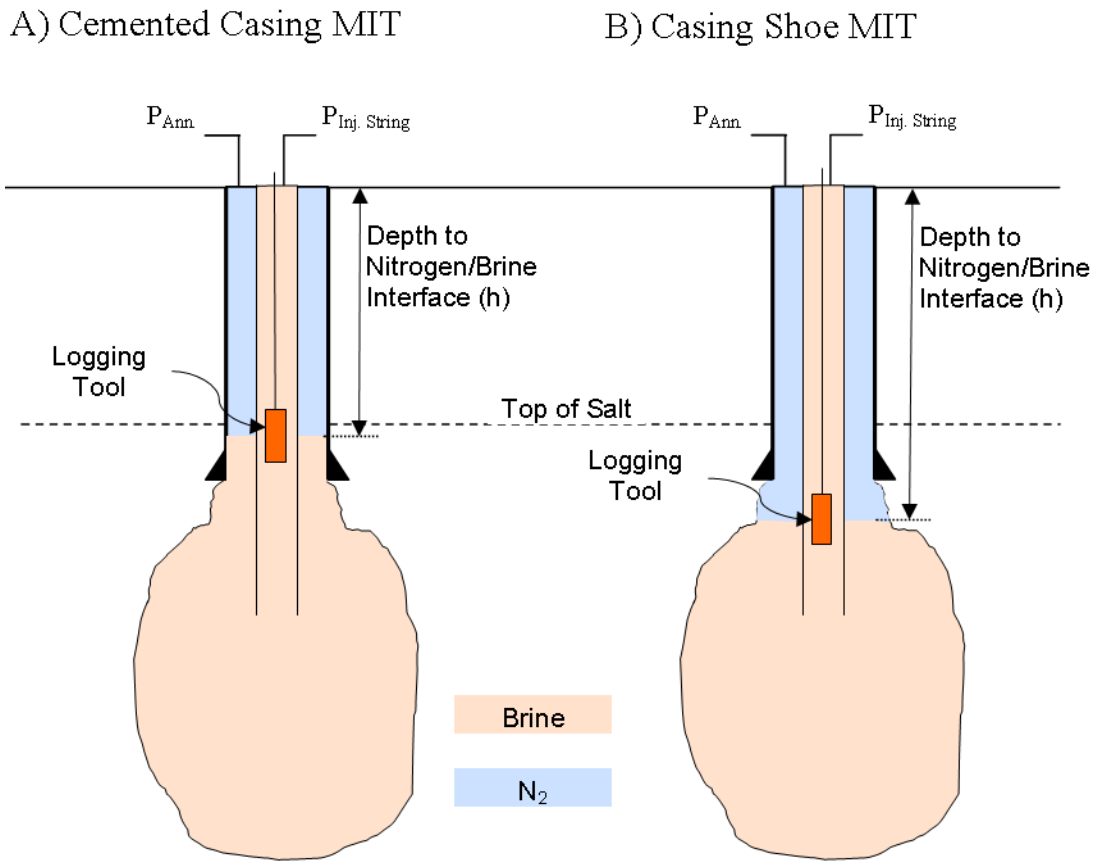

Figure 2 Visual description of the two tests performed during a NBT: (A) the Cemented Casing MIT and (B) the Casing Shoe MIT (not to scale).

The initial test (during a NBT) of the cemented casing is referred to as the Cemented Casing MIT, which tests for internal integrity between the injection string and surrounding annulus; this test is conducted by maintaining the nitrogen/brine interface above the casing shoe and calculating the rate of change (with respect to time) in the nitrogen mass/volume. The second test (during a NBT) places the nitrogen/brine interface below the casing shoe and above the cavern roof; this test is known as the Casing Shoe MIT, which tests for external integrity between the storage system and the surrounding environment. The focus of this research is on the accuracy of determining external integrity via a NBT and therefore is focused on aspects of the Casing Shoe MIT. Although procedures for conducting the NBT (which are typically composed of the Casing MIT and Casing Shoe MIT) do vary, a generalized sequence of events and their associated duration are described as:

a) All stored product is removed from the storage system and replaced with saturated brine (Figure 3). The storage system is then pre-pressurized at rate of about 2.5 psi/min with saturated brine, which is stored at the surface, to near test conditions (e.g. a pressure gradient of 0.8 psi/ft at the casing shoe). This step may take several hours to complete depending on the compressibility of the storage system and typically occurs at least 24 hours prior to the start of the NBT to allow for the cavern pressure to stabilize.

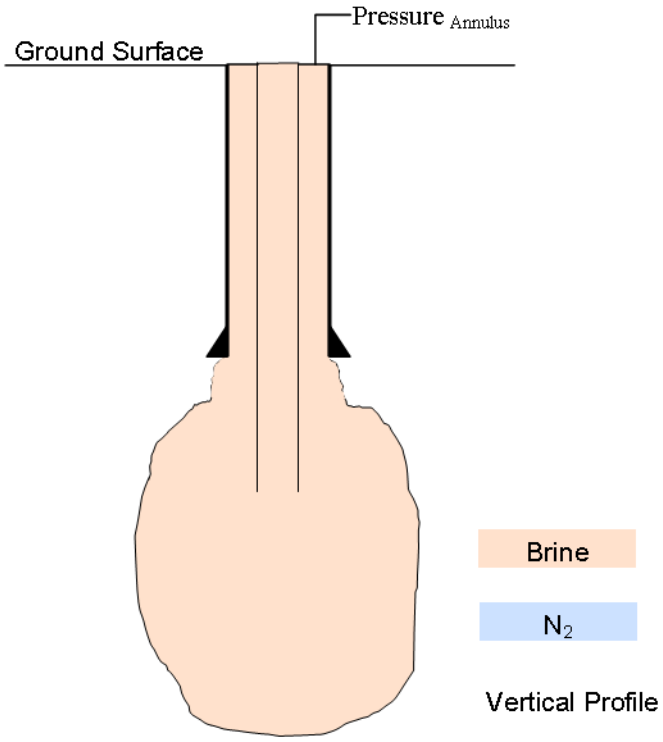

Figure 3 Schematic of storage system during pre-pressurization with saturated brine.

b) An initial temperature survey (base log) is performed from the surface to 50 ft below the expected nitrogen interface via a logging tool located in the injection string (Figure 4).

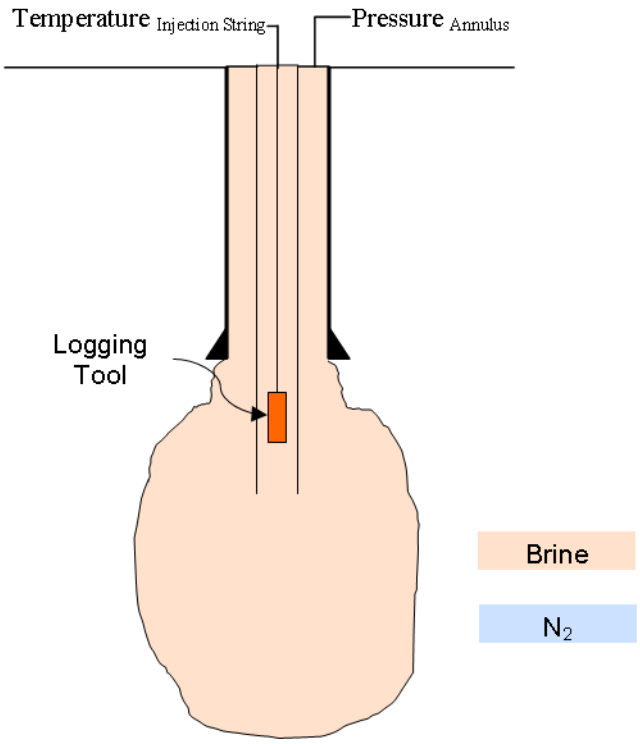

Figure 4 Schematic of storage system during initial temperature log (base log).

c) Nitrogen is then injected into the annulus between the cemented casing and the injection string at the average temperature in the injection string determined from the base log. Nitrogen injection continues until the nitrogen/brine interface is just above the casing shoe and the location of the nitrogen/brine interface is determined via density logging tools positioned in the injection string. This process generally takes approximately one to two hours.

d) The Cemented Casing MIT is performed for approximately an hour, which consists of monitoring pressure at the wellhead and running density logs at the start and finish of the test to monitor the displacement of the nitrogen/brine interface (Figure 5).

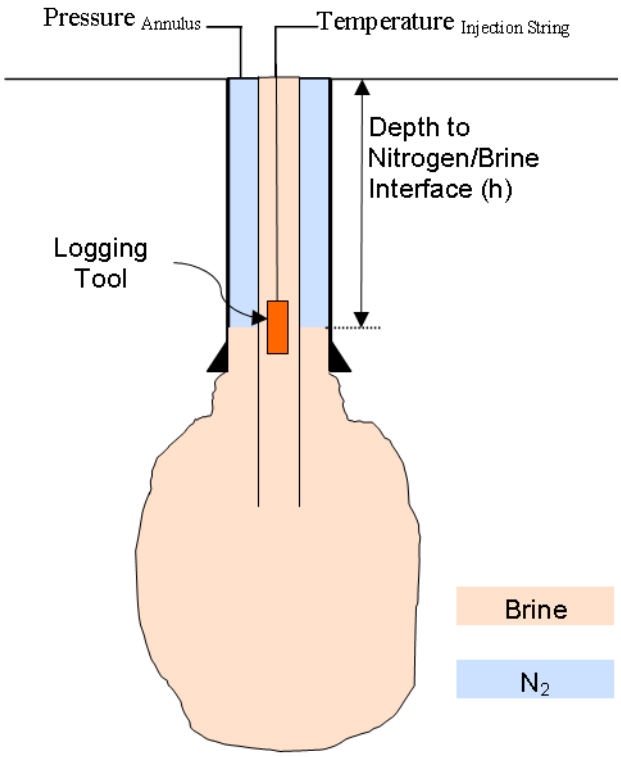

Figure 5 Schematic of storage system during Cemented Casing MIT.

e) After the Cemented Casing MIT has been completed, nitrogen injection into the annular region resumes until the nitrogen/brine interface is below the casing shoe yet above the cavern roof (Figure 6). The second nitrogen injection typically lasts less than one hour.

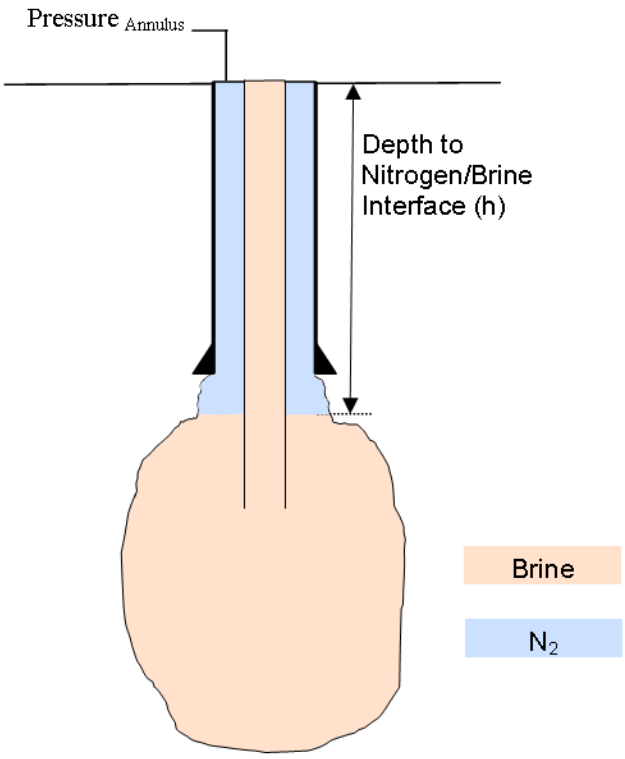

Figure 6 Schematic of storage system at the end of the second nitrogen injection.

f) The Casing Shoe MIT is then performed for no less than 24 hours. Temperature and density logs are performed at the beginning and end of the test period to determine a temperature distribution in the injection string and the displacement of the nitrogen/brine interface depth in the annulus (Figure 7).

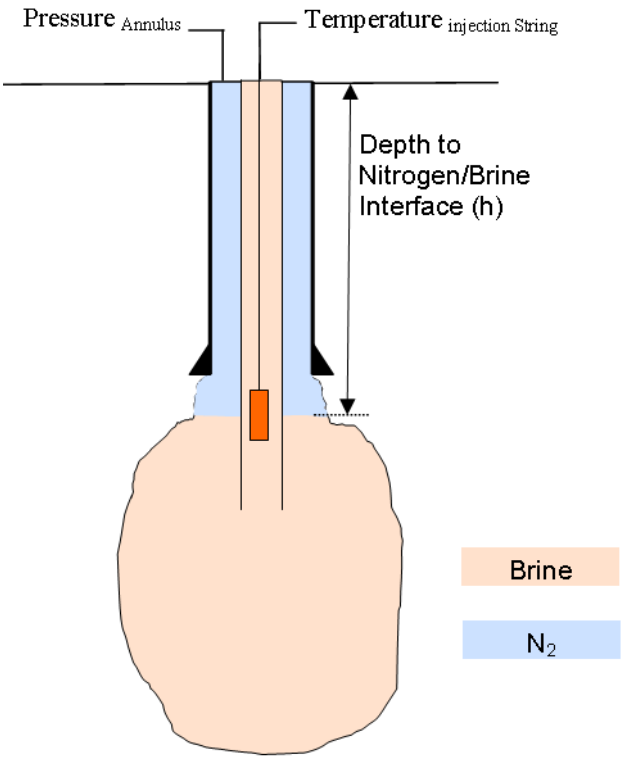

Figure 7 Schematic of storage system during the Casing Shoe MIT.

2.2 Phenomena that Influence the Apparent Leak Rate

Ostensibly, the calculation of an accurate apparent leak (i.e. an apparent leak that is very near the actual leak) may appear to be straightforward; however, there are many phenomena such as: transient heat transfer, salt creep, thermal expansion, rock salt dissolution, adiabatic temperature increase, surface temperature and pressure variations, Earth tides, which may affect the accuracy of the apparent leak rate to varying extents. The goal of this report is to describe how the transient heat transfer phenomena may cause appreciable differences between the calculated apparent leak rate and the actual leak rate.

2.3 Calculation of the Apparent Leak Rate

The mass/volume of nitrogen in the well annulus may be estimated using (1) the measured nitrogen annulus pressure at the wellhead, (2) the knowledge of the annular cross-sectional area as a function of depth, (3) the depth of the nitrogen/brine interface obtained from a logging tool, and (4) the assumption that the brine temperature in the injection string (obtained from a logging tool) is representative of the nitrogen temperature in the annular region adjacent to the injection string. Calculation of nitrogen mass/volume is performed at the start and finish of the test, and

an apparent leak (if any) may be calculated using the starting and final calculated mass/volume values between the two logging campaigns. If the temperature of nitrogen in the annulus is well represented by the brine temperature in the injection string, an accurate leak calculation may be made; however, if the nitrogen temperature is not well represented by the brine temperature the apparent leak calculation may have a large value of error relative to the actual leak rate. Also, large variations in the apparent leak calculations are believed to occur when the temperature of brine (stored on the surface in a brine pond prior to injection) injected into the storage-system during prepressurization or the temperature of nitrogen injected into the annulus differ noticeable from the in situ temperature of the local rock mass, causing the storage system to undergo significant thermal transients. The focus of this research is to determine how variations of well geometry and surface conditions (and associated brine and nitrogen injection temperatures) affect the calculation of an apparent leak.

3 Technical Approach

In an attempt to further understand the transient nature of the heat transfer phenomena associated with a NBT, finite element (FE) modeling was employed to simulate the thermal events during a NBT on a variety of storage well (specifically the well portion of a storage system above the cavern roof) geometries and surface conditions. The thermal analyses were then validated via comparisons of temperature logs taken during a recorded Field Test. The results from the thermal analysis were employed to calculate the apparent and actual leak rates (at the casing shoe temperature and pressure) associated with each of the simulated scenarios.

3.1 Thermal Modeling Computer Program

The finite element computer program SPECTROM-45 (SPE-45) was used to analyze the thermal nature of the NBT on the modeled storage wells. The SPE-45 code is part of the SPECTROM (Special Purpose Engineering Codes for Thermal ROck Mechanics) series of special purpose finite element programs and is capable of modeling two dimensional conductive heat transfer and coupled convective-conductive heat transfer in laminar flow [Svalstad, 1989]. SPE-45 is a uses the Galerkin Finite Element Method (GFEM) with eight-noded serendipity elements to formulate a numerical solutition.

3.2 Equations Implemented by the Thermal Model

Equations 1 through 3 were implemented by SPE-45 to perform the thermal analysis of the storage system and adjacent strata. The dominant heat transfer mechanisms present, during a NBT, having thermal effects on the storage well and surrounding strata are conduction and forced convection. The two-dimensional (axisymmetric) governing equation describing these heat transfer mechanisms acting on the dynamic fluids present in the storage well is:

(Equation 1)

$$\frac{k}{\rho c}\left(\frac{\partial^2 T}{\partial z^2}+\frac{1}{r}\frac{\partial T}{\partial r}+\frac{\partial^2 T}{\partial r^2}\right)-V_z\frac{\partial T}{\partial z}=\frac{\partial T}{\partial t}$$

where:

r	=	radial coordinate direction
z	=	vertical coordinate direction
t	=	time
T(r,z,t)	=	temperature in fluid materials at location (r,z) at time t
k	=	thermal conductivity of fluid
ρ	=	mass density of fluid
c	=	specific heat capacity of fluid at constant pressure
$V_z(r)$	=	vertical velocity of fluid at distance r from the axis of symmetry

Thermally induced (natural) convection was not accounted for during the thermal analysis because it had been determined to not significantly influence the thermal nature of the system, the basis for this assumption is provided in Appendix A.

Fluid flows in the well annulus and injection string were modeled by SPE-45 as laminar vertical flows (i.e. no turbulent flow) through a duct; however, the reduced mean velocity of a turbulent flow was accounted for and the respective velocity profiles were approximated from empirical correlations of an annular velocity profile [Meter and Bird, 1961] (Figure 8) and an axisymmetric velocity profile [Finnemore and Franzini, 2002] (Figure 9); each are quadratic in nature and have the generalized form of:

$$V_z(r) = V_{con} + ar + br^2 \qquad \text{(Equation 2)}$$

where:

r	=	radial coordinate direction
a	=	linear coefficient
b	=	quadratic coefficient
V_{con}	=	Constant term
$V_z(r)$	=	vertical velocity of fluid at radial distance r from axis of symmetry

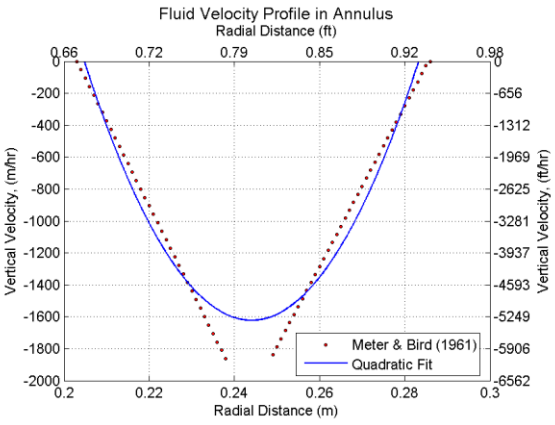

Figure 8 Discrete empirical approximation of the annular velocity profile (red) and continuous quadratic fit (blue).

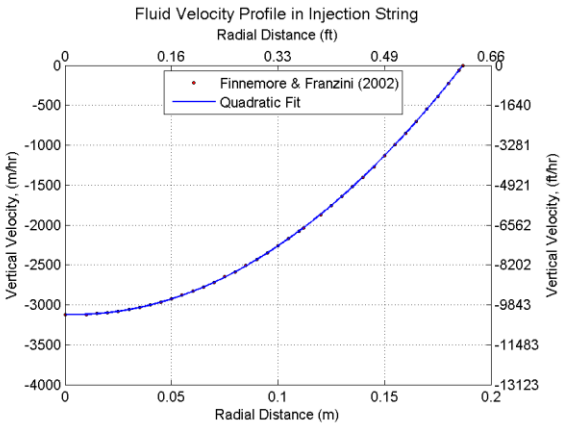

Figure 9 Discrete empirical approximation of an axisymmetric velocity profile (red) in the injection string and continuous quadratic fit (blue).

The governing heat transfer equation for static fluid materials in the storage well and all solid materials in and around the storage well is:

(Equation 3)

$$D\left(\frac{\partial^2 T}{\partial z^2}+\frac{1}{r}\frac{\partial T}{\partial r}+\frac{\partial^2 T}{\partial r^2}\right)=\frac{\partial T}{\partial t}$$

Where:

r	=	radial coordinate direction
z	=	vertical coordinate direction
t	=	time
D	=	thermal diffusivity of solid material (k/ρc)
T(r,z,t)	=	temperature in solid materials at location (r,z) and at time t

3.3 Equations Implemented for the Volume Analysis

A finite difference code was developed to employ Equations 4 through 9 and results from the thermal analysis were implemented to solve for the apparent leak in the modeled storage system. Nitrogen volume in the storage-well annulus was calculated according to the non-ideal gas equation [Cengel and Boles, 2006]:

(Equation 4)

$$PV = m\frac{R_u}{M}ZT$$

Where:

P	=	absolute pressure of gas
V	=	volume of gas
m	=	mass of gas
R_u	=	universal gas constant
M	=	molar mass of gas
Z(P,T)	=	compressibility factor of gas at P and T
T	=	absolute temperature of gas

The compressibility factor (Z), which is a non-linear function of both temperature and pressure was determined from [Sage and Lacey, 1950]:

(Equation 5)

$$Z = AP^2 + BP + C$$

where:

P	=	absolute pressure of gas
A(P,T)	=	quadratic coefficient that is a function of P and T
B(P,T)	=	linear coefficient that is a function of P and T
C(P,T)	=	constant coefficient that is a function of P and T
Z(P,A,B,C)	=	Compressibility factor that is a function of P,A,B, and C
T	=	absolute temperature of gas

Further details on the calculation of the compressibility factor (Z) are given in Appendix B. Equation 4 may be rearranged to solve for gas density:

(Equation 6)

$$\rho = \frac{P}{RZT}$$

Where:

P	=	absolute pressure of gas
R	=	specific gas constant (R_u/M)
T	=	absolute temperature of gas
ρ	=	mass density of gas (m/V)
Z(P,T)	=	compressibility of gas

The approximate change of pressure on a gas over a finite vertical distance may be determined by:

(Equation 7)

$$P_2 = P_1 + \rho_1 gh$$

where:

g	=	gravitational constant
h	=	vertical distance between point 1 and 2
ρ_1	=	mass density of gas at point 1
P_1	=	pressure of gas at point 1
P_2	=	approximation of gas pressure at point 2

The compressibility factor of a gas at standard temperature and pressure (STP) is equal to unity, by recognizing this and making reference to STP conditions, Equation 4 may be manipulated to provide a mass consistent volume calculation by:

(Equation 8)

$$\frac{PV}{ZT} = mR = \frac{P_{STP}V_{STP}}{T_{STP}}$$

where:

P_{STP}	=	standard absolute pressure : 0.101 MPa or 14.7 psia
T_{STP}	=	standard absolute temperature: 293.15 K or 528 R
V_{STP}	=	volume of gas at T_{STP} and P_{STP}
m	=	constant mass of gas
R	=	specific gas constant
P	=	absolute pressure on gas
V	=	volume of gas
T	=	absolute temperature of gas
Z(T,P)	=	compressibility factor of gas at T and P

A similar relationship as shown in Equation 8 may be used to calculate the pressure needed to maintain a mass/volume of gas at a different temperature and pressure:

(Equation 9)

$$\frac{P^1V}{Z^1T^1} = mR = \frac{P^2V}{Z^2T^2}$$

where:

P^1	=	absolute pressure of gas at time 1
T^1	=	absolute temperature of gas at time 1
$Z^1(T^1,P^1)$	=	compressibility factor of gas at T^1 and P^1
m	=	constant mass of gas
R	=	specific gas constant
P^2	=	absolute pressure of gas at time 2
T^2	=	absolute temperature of gas at time 2
V	=	constant volume of gas
$Z^2(T^2,P^2)$	=	compressibility factor of gas at T^2 and P^2

Equation 9 may be used to calculate the pressure on a mass of gas as the temperature varies in time but the volume of the gas is held constant.

4 Thermal Modeling Procedure

The thermal modeling performed during this research consisted of simulating 9 wells (one at a time) each having a unique well architecture and uncased borehole dimension; each of the nine well/borehole combinations were modeled with two different brine surface temperature conditions; resulting in 18 different unique FE models. The domain extent of all FE models was 7 meters in the radial direction and 1000 meters in the vertical direction and was composed of 4429 nodes associated with 1400 eight-noded elements.

4.1 Time Domain

A theoretical NBT was developed for implementation into each of the 18 FE models for thermal analysis. The theoretical NBT (Table 1) accounted for all events that occur during a typical NBT on a storage system.

Table 1 Description, step number, and duration of events included in the FE model of a NBT.

Event Description	Step Number	Event Duration (hours)	Cumulative Duration (hours)
Pre-Pressurization with Brine	I	15	15
Initial Stabilization Period	II	48	63
Initial N_2 Injection	III	1.5	64.5
Cemented Casing MIT	IV	0.75	65.25
Final N_2 Injection	V	0.5	65.75
Final Stabilization Period	VI	24	89.75
Casing Shoe MIT	VII	24	113.75

4.2 Physical Domain

The general well components, adjacent strata, and vertical limits (Figure 10) did not vary between the 18 FE models; however, the radial limits of the well components and open borehole were modified between models. The casing system associated with the storage well [Thoms and Gehle, 1984], and adjacent geology [Kelsall and Nelson, 1983] was typical of that found in the Gulf Coast region. The storage system was assumed to be axisymmetric about the center line of the injection string and was therefore modeled as such (Figure 11).

The uniquely dimensioned storage wells and associated casing architecture of the well are referred to as (in order of increasing radial extent) the Small (Table 2), Medium (Table 3), and Large (Table 4) wells. The open borehole sizes for each well are referred to as (in order of

increasing radial extent) Small, Medium, and Large (Table 5) also. The percentage of total well volume contained in the open borehole of each model is listed in Table 6. The volume of each well/uncased-borehole combination modeled is shown in Appendix C

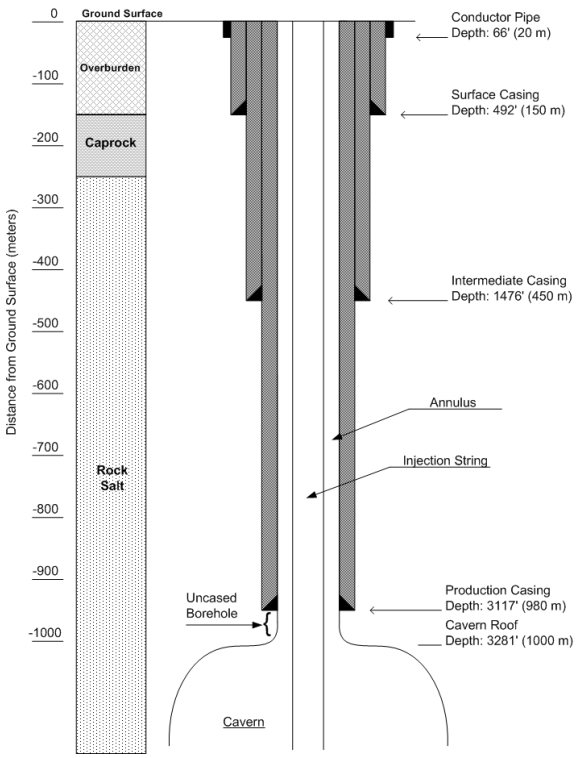

Figure 10 Schematic diagram of the storage well casing system and adjacent strata.

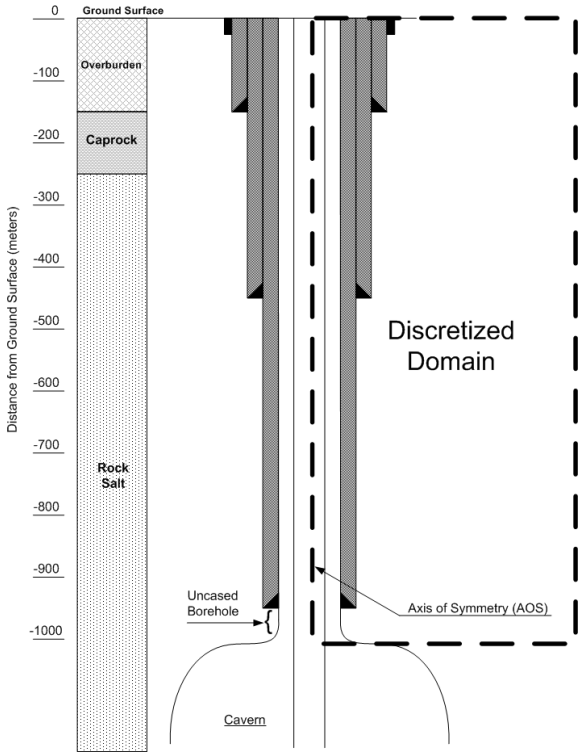

Figure 11 Detail of the discretized domain implemented into the finite element model.

Table 2 Dimensions of the casing system associated with the Small well.

Small Well	**Inside Diameter**		**Outside Diameter**		**Wall Thickness**		**Length**	
	meter	inch	meter	inch	meter	inch	meter	feet
Conductor	0.57	22.50	0.61	24.00	0.02	0.75	20	66
Surface Casing	0.45	17.76	0.47	18.63	0.01	0.44	150	492
Intermediate Casing	0.32	12.70	0.36	14.00	0.02	0.65	450	1476
Production Casing	0.23	8.92	0.24	9.63	0.01	0.35	980	3215
Brine Injection String	0.16	6.28	0.18	7.00	0.01	0.36	1000	3281

Table 3 Dimensions of the casing system associated with the Medium well.

Medium Well	**Inside Diameter**		**Outside Diameter**		**Wall Thickness**		**Length**	
	meter	inch	meter	inch	meter	inch	meter	feet
Conductor	0.57	22.50	0.61	24.00	0.02	0.75	20	66
Surface Casing	0.49	19.12	0.51	20.00	0.01	0.44	150	492
Intermediate Casing	0.39	15.25	0.41	16.00	0.01	0.38	450	1476
Production Casing	0.32	12.62	0.34	13.38	0.01	0.38	980	3215
Brine Injection String	0.22	8.84	0.24	9.63	0.01	0.40	1000	3281

Table 4 Dimensions of the casing system associated with the Large well.

Large Well	**Inside Diameter**		**Outside Diameter**		**Wall Thickness**		**Length**	
	meter	inch	meter	inch	meter	inch	meter	feet
Conductor	1.03	40.50	1.07	42.00	0.02	0.75	20	66
Surface Casing	0.88	34.50	0.91	36.00	0.02	0.75	150	492
Intermediate Casing	0.72	28.50	0.76	30.00	0.02	0.75	450	1476
Production Casing	0.57	22.50	0.61	24.00	0.02	0.75	980	3215
Brine Injection String	0.37	14.69	0.41	16.00	0.02	0.66	1000	3281

Table 5 Open borehole dimensions for each of the three well sizes.

Well Description	Production Casing (ID)		Diameter of Open Borehole					
			Small Borehole		Medium Borehole		Large Borehole	
	meter	inch	meter	inch	meter	inch	meter	inch
Small Well	0.23	8.9	0.32	12.5	0.91	36	1.22	48
Medium Well	0.32	12.6	0.44	17.5	0.91	36	1.22	48
Large Well	0.57	22.5	0.71	28.0	1.25	49	1.89	74

Table 6 Percentage of well volume contained in the open borehole for each well and borehole size.

Well Description	Open Borehole Description		
	Small Borehole	Medium Borehole	Large Borehole
Small Well	7%	45%	60%
Medium Well	6%	27%	40%
Large Well	4%	15%	30%

4.3 Material Properties

The thermal analyses each included seven materials, each material and the associated thermophysical properties implemented into the FE models are shown in Table 7. The physical properties of nitrogen are highly dependent on both temperature and pressure (Appendix D); however, during the thermal analysis a reference state of 12.5 MPa and 35 °C was used during the thermal analysis of this research. The temperature dependency of salt thermal conductivity was neglected during the thermal analysis.

Table 7 Materials included in FE analysis and associated thermophysical properties.

Material	Density (ρ) kg/m³	Heat Capacity (c_p) W-hr/kg-K	Thermal Conductivity (k) W/m-K	Reference
Nitrogen Gas	129	0.337	0.033	[NIST, 2010]
Rock Salt	2160	0.214	5.000	[Kelsall & Nelson, 1983]
Brine (25% NaCl)	1189	0.913	0.575	[Dittman, 1977]
Steel	8009	0.128	865.4	[Ratigan & Blair, 1994]
Caprock	2899	0.238	5.296	[Ratigan & Blair, 1994]
Grout	2323	0.186	2.163	[Ratigan & Blair, 1994]
Overburden	2195	0.222	3.306	[Ratigan & Blair, 1994]

4.4 Material Locations

The modeled materials and their respective geometries in each of the nine modeled well architectures were dependent on the simulated event (Table 1) and the well architecture. All modeled material geometries were held constant during a single model except for the materials present in the annular space between the injection string and production casing, which were dependent on the simulated event.

During pre-pressurization of the storage system (Step I) and the initial stabilization (Step II) events, the annular space and uncased borehole contained only brine (Figure 12). The annular region was modeled as containing nitrogen gas from the ground surface to a depth of 970 meters (10 meters above the casing shoe) and brine in the annular and uncased-borehole regions from a depth of 970 meters to the lower boundary during the initial nitrogen injection (Step III) and Cemented Casing MIT (Step IV). The final nitrogen injection (Step V), final stabilization period (Step VI), and Casing Shoe MIT (Step VII) were modeled as having the annular region and uncased borehole as containing only nitrogen gas.

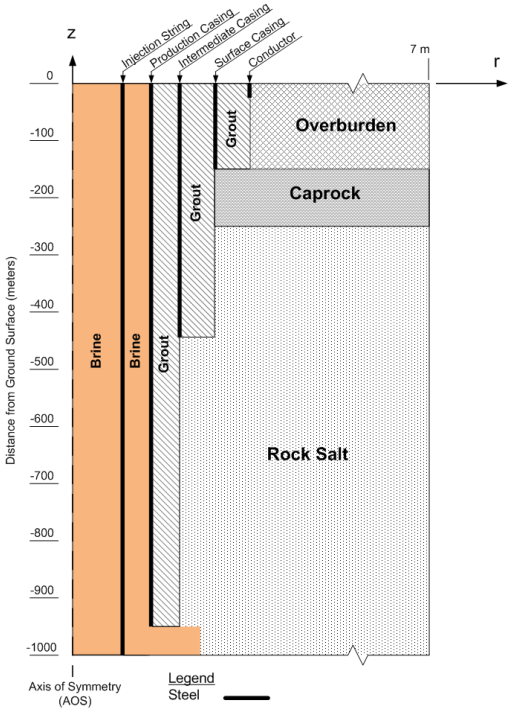

Figure 12 Relative locations of all materials modeled during Steps I and II of the thermal analyses (not to scale).

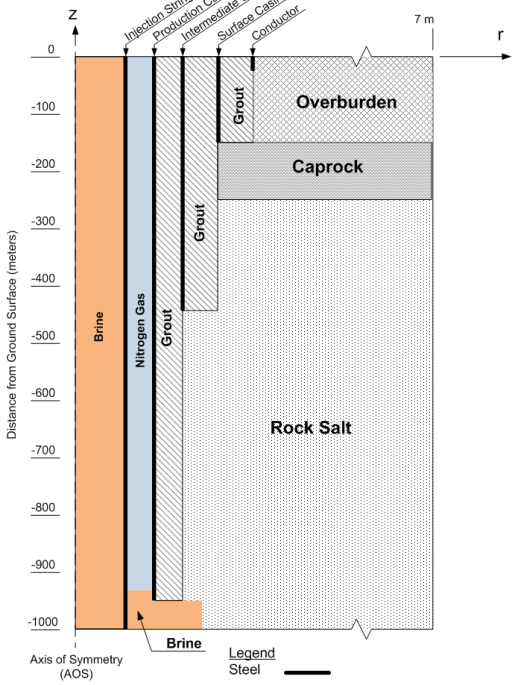

Figure 13 Relative locations of all materials modeled during Steps III and IV of the thermal analyses (not to scale).

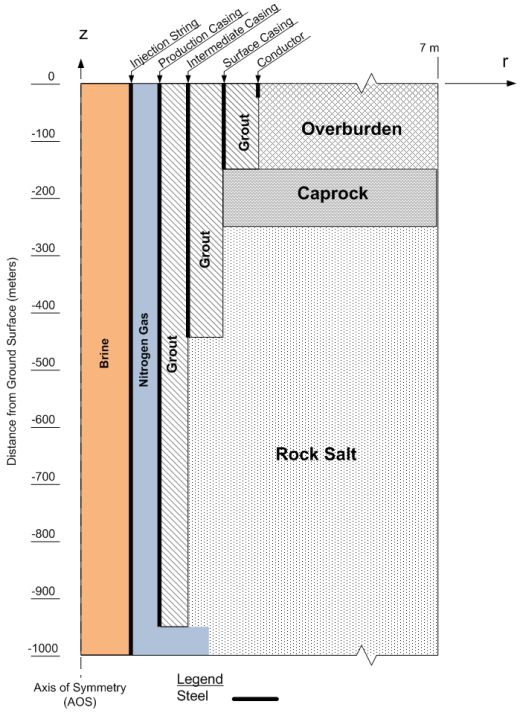

Figure 14 Relative locations of all materials modeled during Steps V, VI, and VII of the thermal analyses (not to scale).

4.5 Velocity Profiles

The brine injection rate for each of the three well sizes was determined by assuming (1) the injection rate was at a 1 psi/min on the injection string, (2) the storage-system compressibility was 84.1 m^3/MPa (36 bbls/psi), and (3) the injection string dimensions were as described in Table 2, Table 3, and Table 4. The mean velocity, calculated from the injection rate, was then used to determine with empirical correlations components of the velocity profiles, which were quadratic in nature (Table 8).

The velocity profiles of nitrogen during Steps III (Table 8) and V (Table 9) were determined using an assumption of the average velocities in the annulus were respectively 650 and 60 m/hr; also that the annular dimensions of the wells and uncased boreholes were as described in Table 2, Table 3, Table 4, and Table 5.

Table 8 Coefficients of the velocity profiles employed during steps I and III.

Well Size	*Event Number	V_{con}	A	B
Small	I	-1.72E+04	-1.31E+04	3.01E+06
Small	III	3.56E+04	-7.13E+05	3.53E+06
Medium	I	-8.66E+03	-3.64E+03	7.23E+05
Medium	III	4.18E+04	-6.03E+05	2.14E+06
Large	I	-3.12E+03	-8.12E+02	9.37E+04
Large	III	6.12E+04	-5.15E+05	1.06E+06

* I: Pre-Pressurization with Brine
III: Initial N_2 Injection

Table 9 Coefficients used for quadratic velocity profile of nitrogen during Step V for each well/borehole size.

Well Size	Uncased Borehole Size	*Event Number	V_{con}	A	B
Small	Small	V	1.63E+02	-2.84E+03	1.14E+04
Small	Medium	V	1.83E+01	-2.25E+02	4.10E+02
Small	Large	V	1.27E+01	-1.44E+02	2.05E+02
Medium	Small	V	2.29E+02	-2.89E+03	8.40E+03
Medium	Medium	V	4.67E+01	-4.31E+02	7.46E+02
Medium	Large	V	2.83E+01	-2.56E+02	3.52E+02
Large	Small	V	5.19E+02	-3.98E+03	7.14E+03
Large	Medium	V	1.23E+02	-7.72E+02	9.38E+02
Large	Large	V	6.24E+01	-3.47E+02	3.05E+02

* V: Final N_2 Injection

4.6 In Situ Temperature Distribution

Two different temperature distributions were implemented into the thermal analyses that represented in situ temperature conditions when the surface temperature was 7 °C (Figure 15) and 35 °C (Figure 16). The surface temperature values were chosen to represent the yearly averaged low and high temperature during the coolest and warmest months in the gulf coast region of the United States [NOAA]. The two distributions were identical from a depth of 10 meters to the lower boundary, but varied in the upper 10 meters depending on the nature of the simulated surface temperature. A constant temperature of 25 °C was chosen at a depth of 10 meters below the ground surface [SMU Geothermal Database]. Based on the modeled strata, typical in situ temperature gradients (Table 10) were then applied to obtain a temperature distribution to be used as a far-field boundary condition [Van Sambeek et al., 2005].

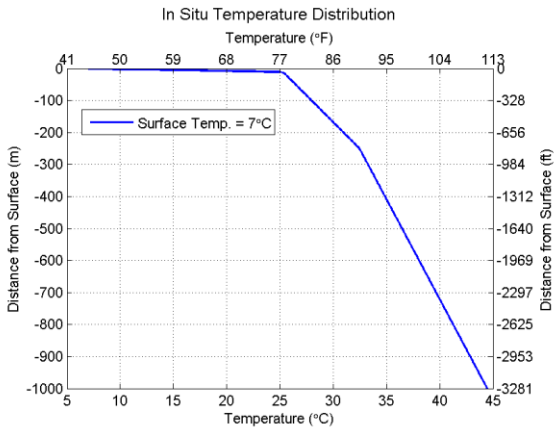

Figure 15 In situ temperature distribution when the ground surface temperature equaled 7 °C.

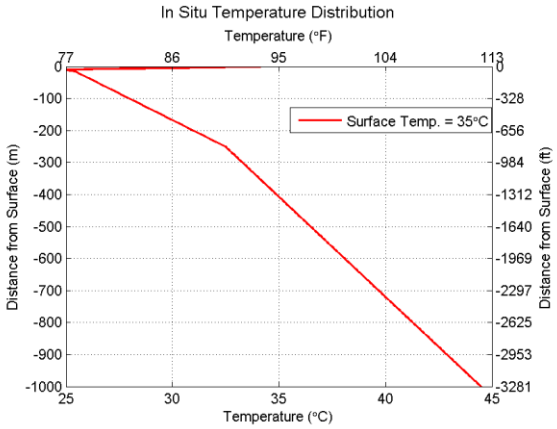

Figure 16 In situ temperature distribution when the ground surface temperature equaled 35 °C.

Table 10 Modeled in situ temperature gradients.

Material	Temperature Gradient (°C/m)
Overburden	0.03
Caprock	0.016
Rock Salt	0.016

4.7 Initial Conditions

Initial conditions for the thermal analysis were found by applying the appropriate far-field boundary condition to the domain and solving for the steady-steady temperature distribution. A constant temperature (Dirichlet) boundary condition (BC) on the upper and right boundaries of the domain, where the upper BC was either 7 °C (Figure 17) or 35 °C (Figure 18) and the corresponding in situ temperature distribution was defined at the right boundary. The left and lower boundaries of the domain were assigned an insulated (Neumann) boundary condition, as the left boundary represents the axis of symmetry (by definition a zero flux boundary) and the lower boundary is an artificial boundary (i.e. the true physical domain does not end at the cavern roof).

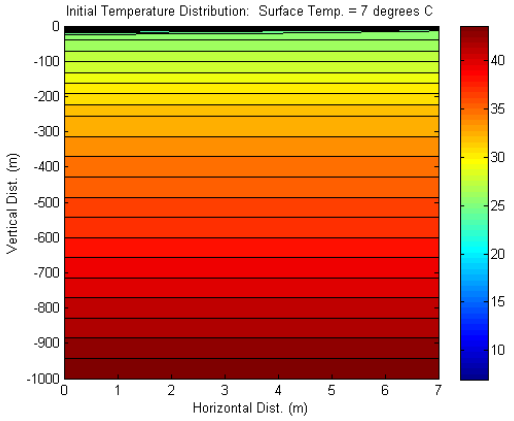

Figure 17 Initial temperature distribution of the model domain with of surface temperature of 7 °C, computed by SPECTROM-45.

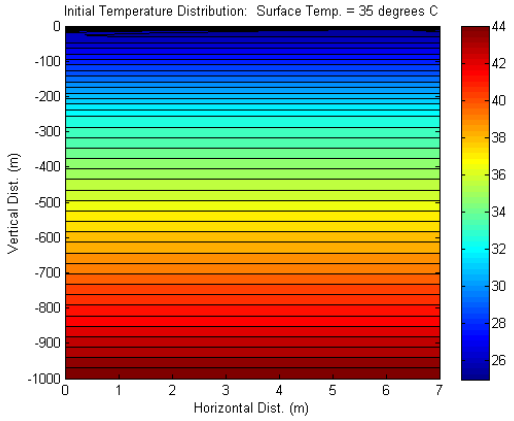

Figure 18 Initial temperature distribution of the model domain with of surface temperature of 35 °C, computed by SPECTROM-45.

4.8 Boundary Conditions

Two types of boundary conditions were used during the thermal analyses, those were the Neumann or insulated type (Γ_N) and the Dirichlet or fixed temperature type (Γ_D). The locations where specific boundary conditions were applied are shown in Figure 19, the step number and the associated boundary condition type are listed in Table 11.

The Lower and Left boundary conditions were maintained as a no flux condition throughout all thermal analyses. The Right boundary, at a distance great enough that heat variations caused by injections into the storage well will not affect it (far-field), was fixed temperature values that are shown in Figure 15 or Figure 16 depending on the nature of the initial surface conditions. The Upper boundary condition was assigned a fixed temperature to obtain an initial condition during each thermal analysis, but was then assigned an insulted boundary condition during all proceeding steps to allow the FE model to determine the surface temperature distribution resulting from the modeled events.

The Injection String boundary at the wellhead was assigned a fixed temperature, equal to that of the initial surface temperature, during the initial brine injection (Step I) to simulate brine being injected from surface ponds at the current surface temperature. The injection string was then assigned an insulated boundary condition for all following Steps. The Annular boundary at the wellhead was assigned a fixed temperature during both nitrogen injections (Steps III and IV). The fixed temperature value, for both injections, was equal to the calculated average injection

string temperature at the end of Step II; this was done to simulate the typical NBT procedure. The BC on the annulus at the wellhead was assigned an insulated boundary condition when nitrogen gas was not simulated as being injected.

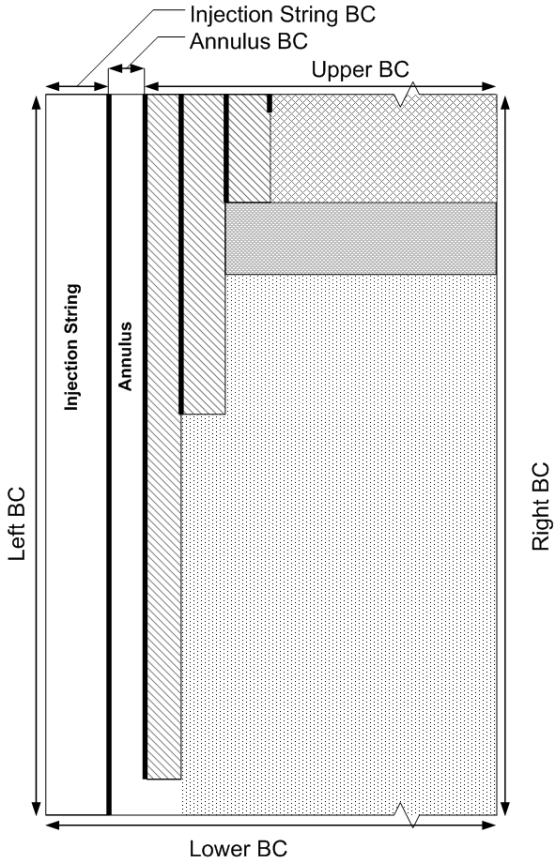

Figure 19 Identification of the six boundary condition locations.

Table 11 Type and location of boundary conditions during each step.

Step Number	Location of Boundary Condition					
	Lower	Right	Upper	Left	Annulus	Injection String
I	Γ_N	Γ_D	Γ_N	Γ_N	Γ_N	Γ_D
II	Γ_N	Γ_D	Γ_N	Γ_N	Γ_N	Γ_N
III	Γ_N	Γ_D	Γ_N	Γ_N	Γ_D	Γ_N
IV	Γ_N	Γ_D	Γ_N	Γ_N	Γ_N	Γ_N
V	Γ_N	Γ_D	Γ_N	Γ_N	Γ_D	Γ_N
VI	Γ_N	Γ_D	Γ_N	Γ_N	Γ_N	Γ_N
VII	Γ_N	Γ_D	Γ_N	Γ_N	Γ_N	Γ_N

Γ_N = Neumann type boundary condition (constant heat flux)

Γ_D = Dirichlet type boundary condition (constant temperature)

5 Thermal Modeling Results

The results from specific steps of the thermal modeling resulted in oscillations with respect to both time and space, the nature of these errors are briefly discussed below. The thermal modeling was performed on 18 unique scenarios, each composed of seven defined steps (Table 1). The results from the Large well with a Large uncased borehole simulated with a brine surface temperature of 7 °C are shown herein.

5.1 Numerical Oscillations (Wiggles)

Numerical oscillations or wiggles were observed during the transient temperature solution during the modeling of Steps I and III in region of the convected fluid (i.e. brine or nitrogen). These anomalous values were the result of the flow having a very high Peclét number (i.e. the ratio of the 'strength' of the convective and diffusive processes was very large), which was the result of the convected fluid material having a high velocity and very low thermal conductivity. Although the wiggles appear to be completely erroneous, because of the nature of the GFEM, these values do not result in a global temperature change but rather a redistribution of it within the convected fluid and thus maintaining a conservation of energy [Gresho and Sani, 1998].

The two regions where wiggles were observed during the thermal modeling were near the moving heating/cooling front in the convected fluid (Figure 20) and at the nitrogen/brine interface (Figure 21). The wiggles near the moving front were the result of the steep temperature gradient caused by the highly convective flow modeled during the thermal analysis. The front translated spatially with time with the fluid and resulted in wiggles that progressed through the domain with time. The other occurrence of wiggles, at the nitrogen/brine interface, was caused by the formation of a steeply graded temperature boundary, just inside of the nitrogen above the interface. Wiggles here again resulted from a lack of thermal diffusion, which if a higher value were modeled would act as a temperature smoothing process that acts to prevent the formation of steep thermal gradients. Consequently, the numerically integrated solution results in sharply graded wiggles that wane in magnitude with time.

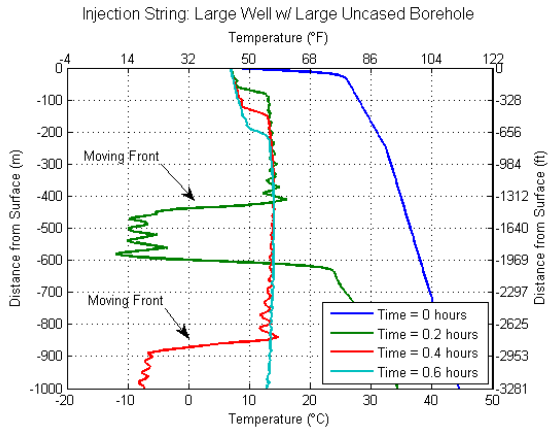

Figure 20 Identification of 'moving font' in the injection string during Step I of the thermal analysis.

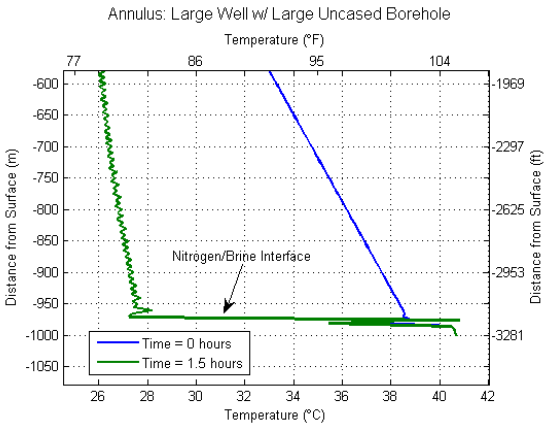

Figure 21 Identification of the nitrogen/brine interface in the annulus during Step III of the thermal analysis.

5.2 Step I

During the initial step of the thermal modeling, brine was simulated as being injected into the injection string from the surface, with a temperature of 7 °C for a duration of 15 hours (Figure 22 and Figure 23). Brine was also simulated in the annular region, but with a zero velocity (Figure 24 and Figure 25). Numerical error was observed, during the initial two hours of Step I, in the injection string temperature. The error was in the form of sharp temperature osillations during the early stages of the step (Figure 23).

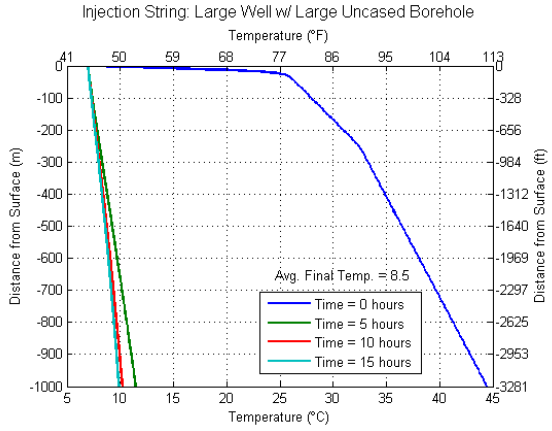

Figure 22 Temperature distributions in the injection string during Step I.

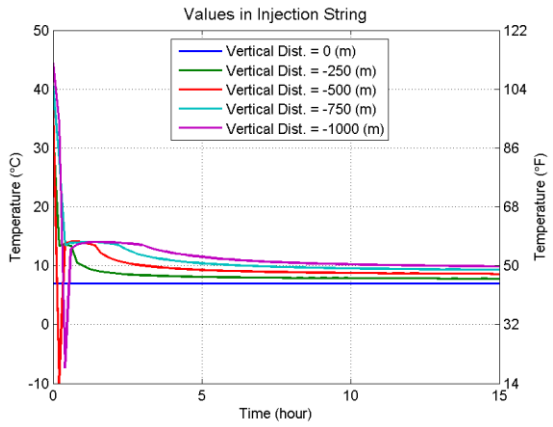

Figure 23 Continuous temperature values at various depths in the injection string during Step I.

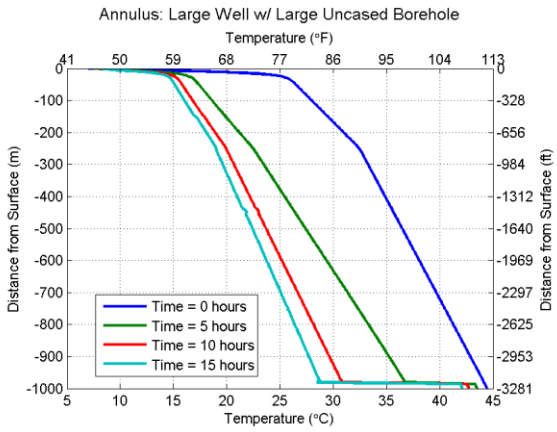

Figure 24 Temperature distribution in the annulus during Step I.

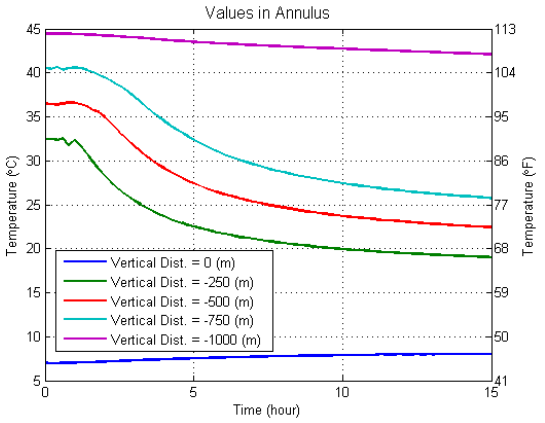

Figure 25 Continuous temperature values at various depths in annulus during Step I.

5.3 Step II

Step II of the thermal modeling simulated the initial stabilization period of the NBT, during which only conductive heat transfer was simulated in the injection string (Figure 26 and Figure 27) and annulus (Figure 28 and Figure 29). The average temperature in the injection string at the end of Step II (26.3 °C) was calculated and implemented as the temperature of the simulated nitrogen injections during Steps III and V.

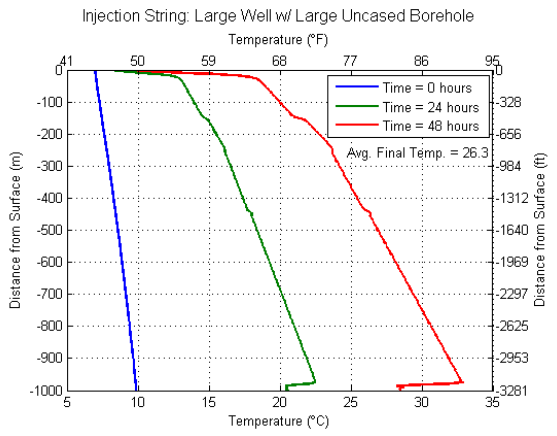

Figure 26 Temperature distributions in the injection string during Step II of the thermal analysis.

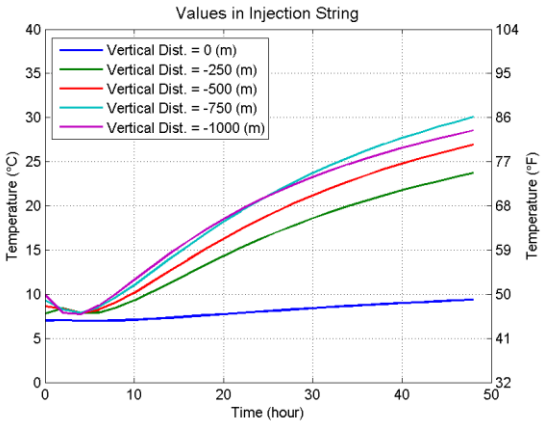

Figure 27 Continuous temperature values at various depths in the injection string during Step II.

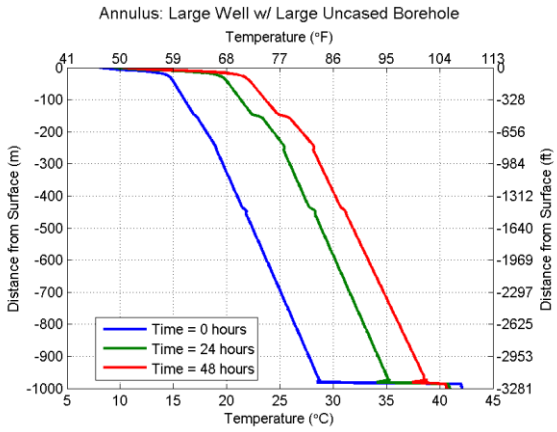

Figure 28 Temperature distributions in the annulus during Step II of the thermal analysis.

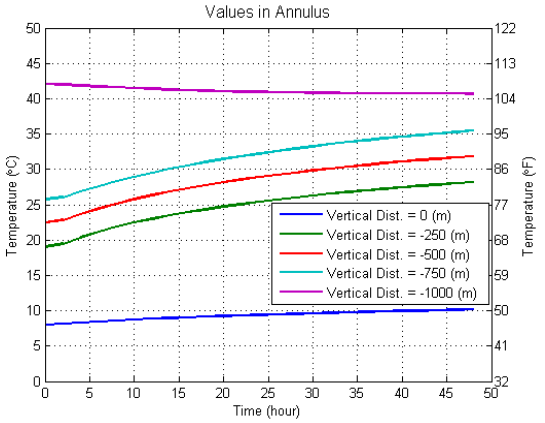

Figure 29 Continuous temperature values at various depths in the annulus during Step II.

5.4 Step III

Step III of the thermal modeling simulated brine as static in the injection string (Figure 30 and Figure 31) and the injection of nitrogen into the annulus (Figure 32 and Figure 33) at a temperature of 26.3 °C (the average temperature in the injections string at the end of Step II) for a duration of 1.5 hours. The nitrogen/brine interface was simulated as being at a distance of 970 below the ground surface in the annulus.

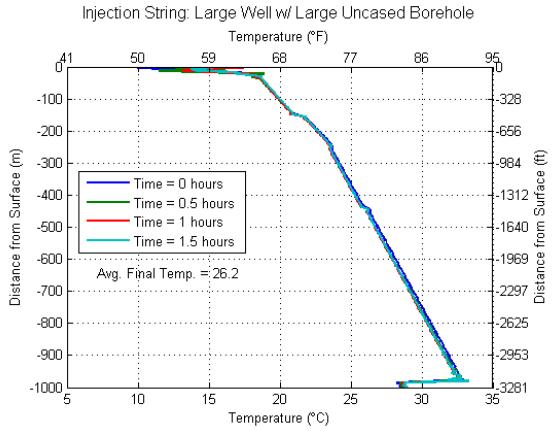

Figure 30 Temperature distributions in the injection string during Step III of the thermal analysis.

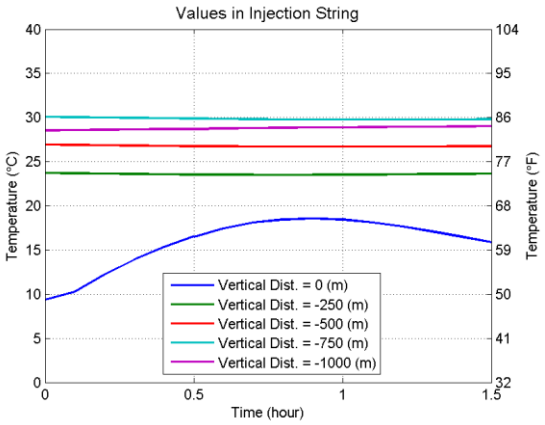

Figure 31 Continuous temperature values at various depths in the injection string during Step III

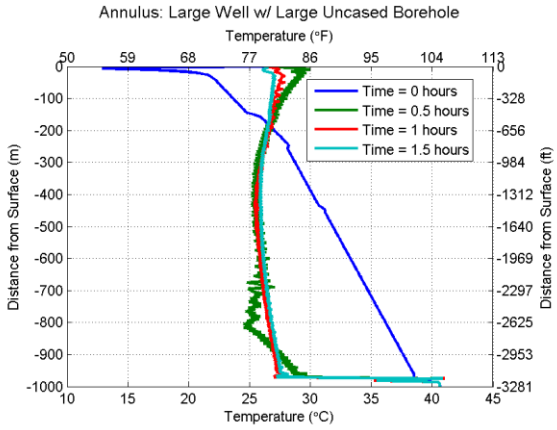

Figure 32 Temperature distributions in the annulus during Step III of the thermal analysis.

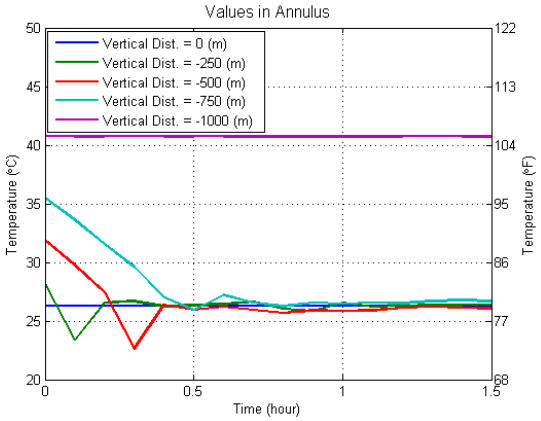

Figure 33 Continuous temperature values at various depths in the annulus during Step III

5.5 Step IV

Step IV of the thermal analysis simulated the 0.75 hour time duration between the two nitrogen injections, during which both the brine in the injection string (Figure 34 Figure 35) and nitrogen/brine in the annulus (Figure 36 and Figure 37) were modeled as being static.

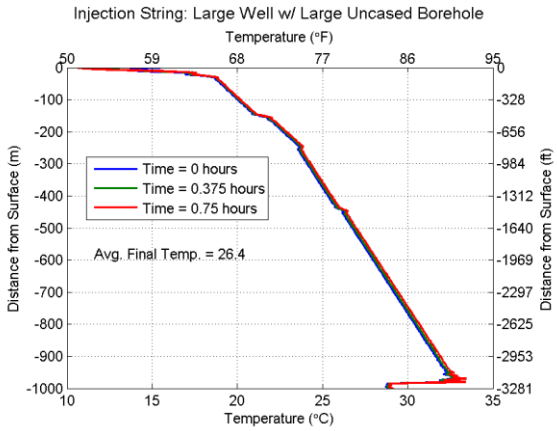

Figure 34 Temperature distributions in the injection string during Step IV of the thermal analysis.

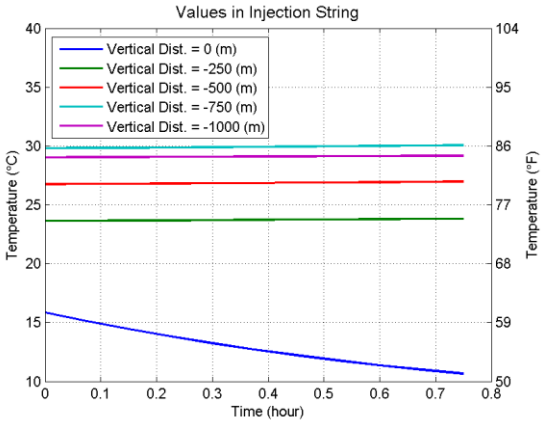

Figure 35 Continuous temperature values at various depths in the injection string during Step IV.

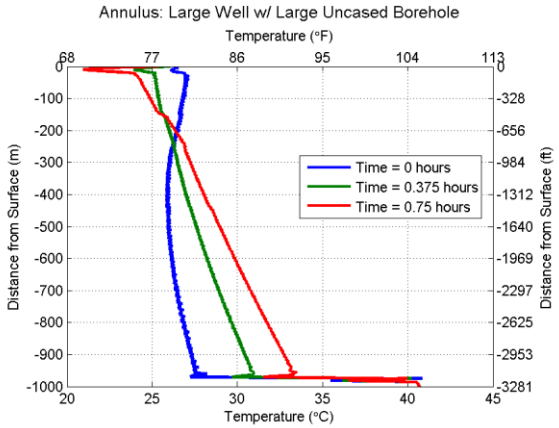

Figure 36 Temperature distributions in the annulus during Step IV of the thermal analysis.

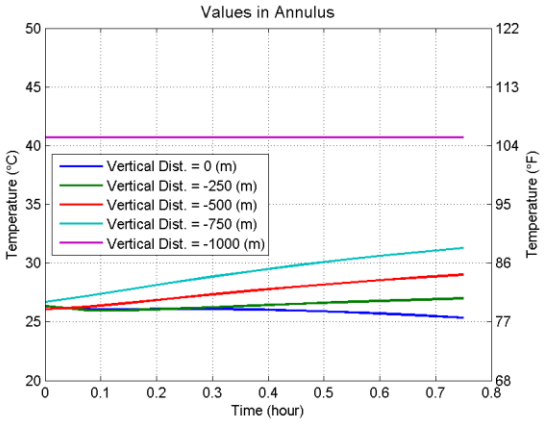

Figure 37 Continuous temperature values at various depths in the annulus during Step IV.

5.6 Step V

Step V of the thermal analysis simulated brine as being static in the injection string (Figure 38 and Figure 39) and simulated the second injection of nitrogen into the well annulus (Figure 40 and Figure 41) for a duration of 0.5 hours. During this step the nitrogen/brine interface was modeled as being at the lower boundary (i.e. the only simulated material in the annulus was nitrogen gas).

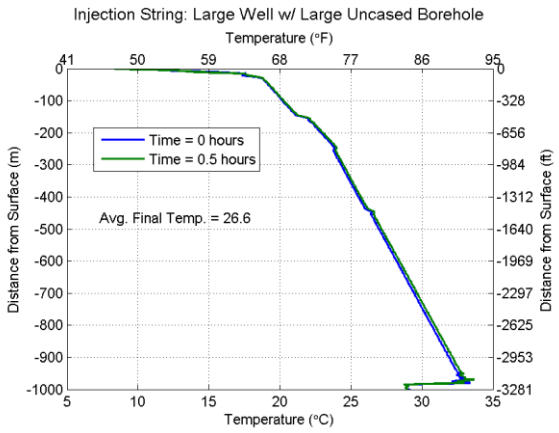

Figure 38 Temperature distributions in the injection string during Step V of the thermal analysis.

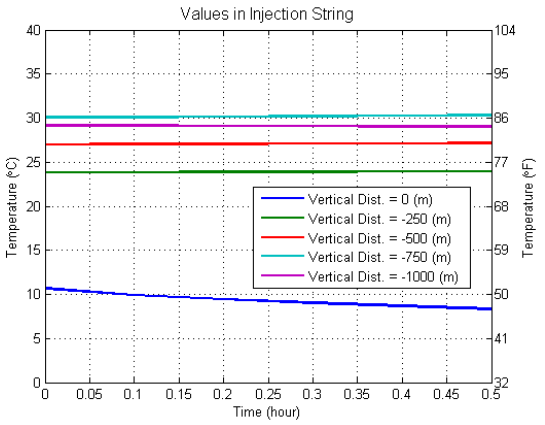

Figure 39 Continuous temperature values at various depths in the injection string during Step V.

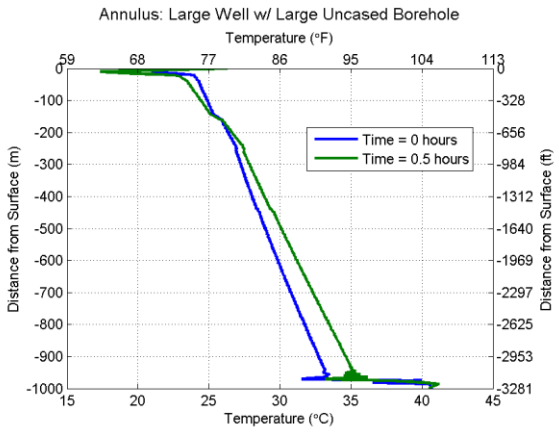

Figure 40 Temperature distributions in the injection annulus Step V of the thermal analysis.

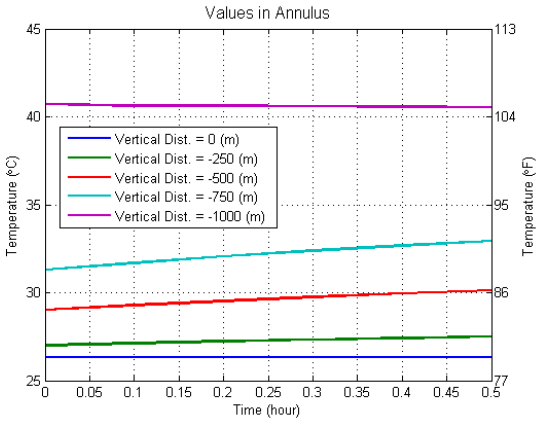

Figure 41 Continuous temperature values at various depths in the annulus during Step V.

5.7 Steps VI and VII

Steps VI and VII included the final stabilization period (initial 24 hours) and the Casing Shoe MIT (final 24 hours), both steps simulated the brine in the injection string (Figure 42 and Figure 43) and nitrogen in the annulus (Figure 44 and Figure 45) as being static. The temperature distributions in the injection string and annulus at the beginning of Step VI and at the steady-state condition are shown in Figure 46 and Figure 47. The temperature distribution at the beginning of Step VI, relative to the steady-state temperature distribution, acts as an indicator to the nature of the transient heat transfer (i.e. will the temperature at a point need to increase or decrease to reach the steady-state value). The difference between the annular and injection string distributions at the beginning of Step VI and at steady state are shown in Figure 48, and the sum of the difference at each time step is shown in Figure 49.

The result data from Figure 46 and Figure 47 indicate that both the injection string and annular temperature distributions will need to warm to reach the steady-state condition. The data from Figure 49 indicates by the large positive value that the cumulative annular temperature is warmer than the cumulative injection string temperature during the 48 hour simulation period. The cumulative annular temperature distribution also warmed at a faster rate than that of the injection string during the initial 3 hours of Step VI (indicated by the positive slope); then from 3 to 48 hours the cumulative injection string temperature began to warm faster than that of the annular(indicated by the negative slope).

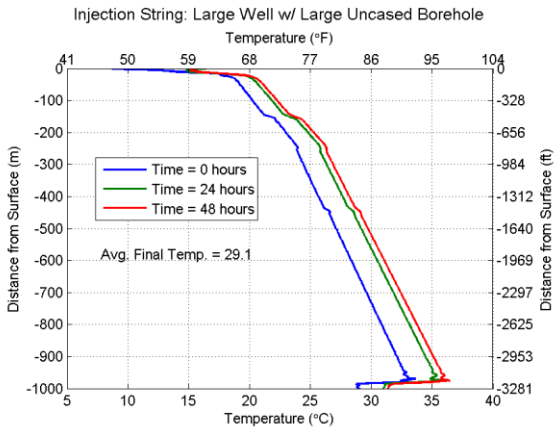

Figure 42 Temperature distributions in the injections string during Steps VI and VII of the thermal analysis.

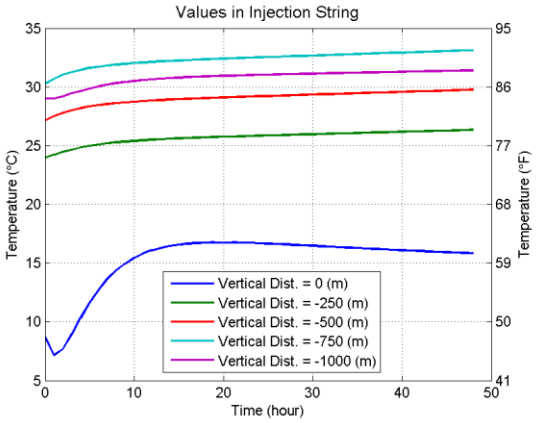

Figure 43 Temperature distribution with time at various depths in the injection string during Steps VI and VII of the thermal analysis.

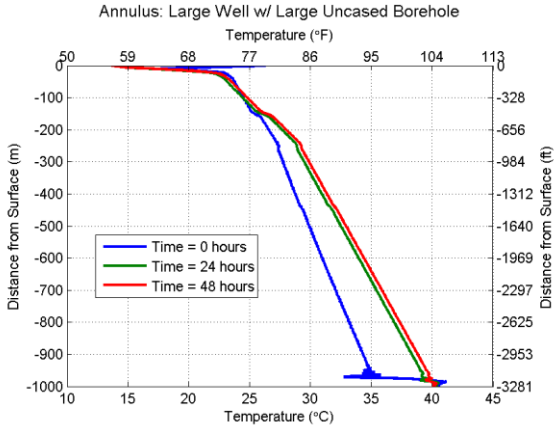

Figure 44 Temperature distribution in the injections annulus Steps VI and VII of the thermal analysis.

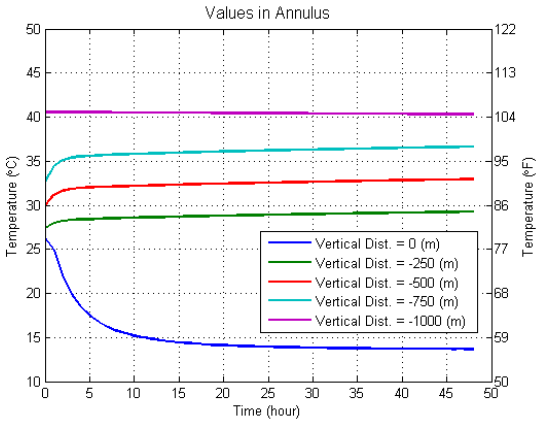

Figure 45 Temperature distribution with time at various depths in the annulus during Steps VI and VII of the thermal analysis.

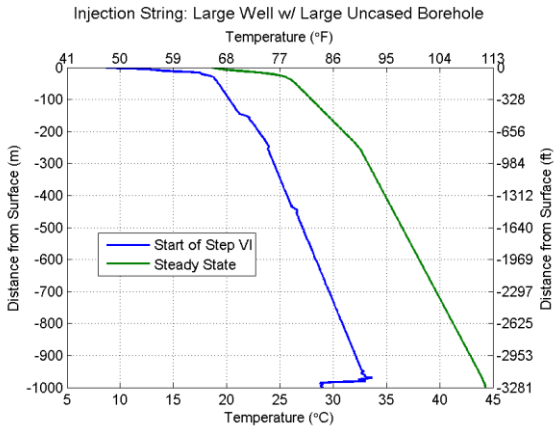

Figure 46 Temperature distributions in the injection string at the start of Step VI and at steady state.

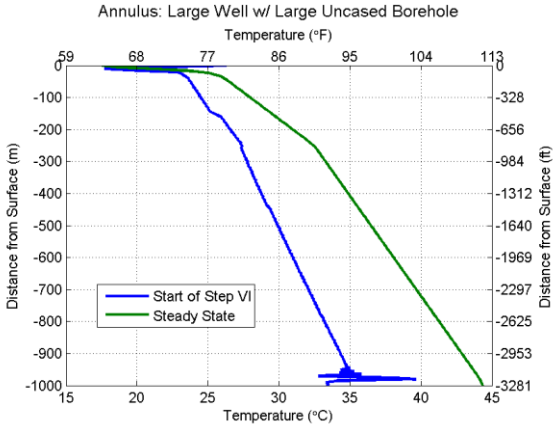

Figure 47 Temperature distributions in the annulus at the start of Step VI and at steady state.

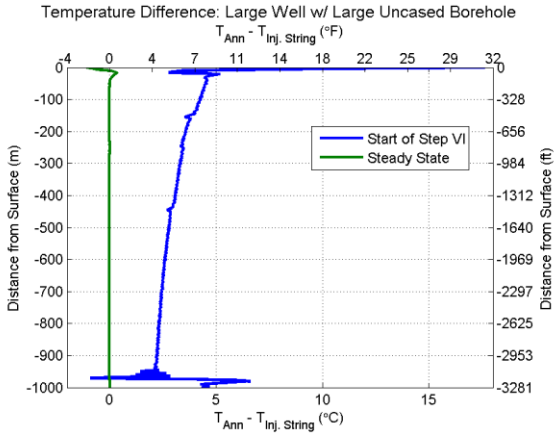

Figure 48 Temperature difference between the annulus and injection string at the start of Step VI and at steady state.

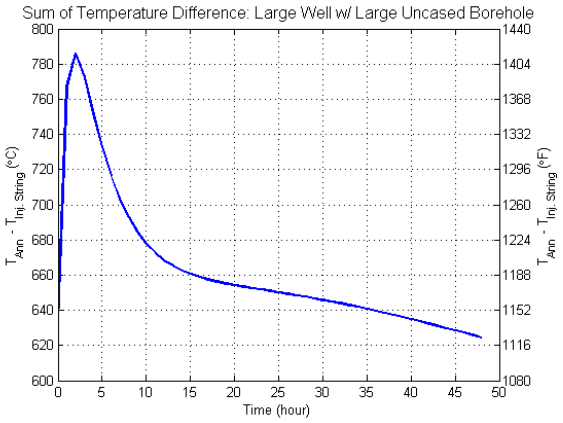

Figure 49 Sum of the temperature difference between the annulus and injection string during Steps VI and VII.

6 Validation of Thermal Model

Validation of the thermal modeling method applied in this research was done by utilizing the temperature logs, site conditions, well geometry, and a chronological list of procedures performed during a NBT on a well owned by a private company. The generic name "Field Test" will be used as a preface in this document when referring to all items pertaining to this obtained data. The Field Test information was implemented into the current thermal modeling scheme and the modeling results were compared to the actual temperature logs of the Field Test.

6.1 Field Test Data

The geometry of the casing architecture associated with the Field Test well is described in Table 12 and the radial extent of the uncased borehole is shown in Table 13. The annular volume of the Field Test well as a function of depth below the ground surface is shown in Figure 50. The temperature distributions recorded in the injection string during the Field Test (Figure 51) were used to assume an in-situ temperature distribution that was be 4 to 6 °C warmer than the final temperature log taken during the Field Test. The duration of Steps I and II of the NBT (Table 14) of the modeling procedure are unknown and were assumed during the validation process. All material properties were assumed to be consistent with those values listed in Table 7.

Table 12 Geometry of casing architecture of the Field Test well.

Field Test Well	**Inside Diameter**		**Outside Diameter**		**Wall Thickness**		**Length**	
	meter	inch	meter	inch	meter	inch	meter	feet
Conductor	0.57	22.50	0.61	24.00	0.02	0.75	20	66
Surface Casing	0.49	19.12	0.51	20.00	0.01	0.44	150	492
Intermediate Casing	0.39	15.25	0.41	16.00	0.01	0.38	450	1476
Production Casing	0.32	12.62	0.34	13.38	0.01	0.38	975	3199
Brine Injection String	0.22	8.84	0.24	9.63	0.01	0.40	980	3215

Table 13 Uncased borehole radial extent of the Field Test well.

Well Description	Production Casing (ID)		Diameter of Uncased Borehole	
	meter	inch	meter	inch
Field Test Well	0.32	12.6	0.80	31.5

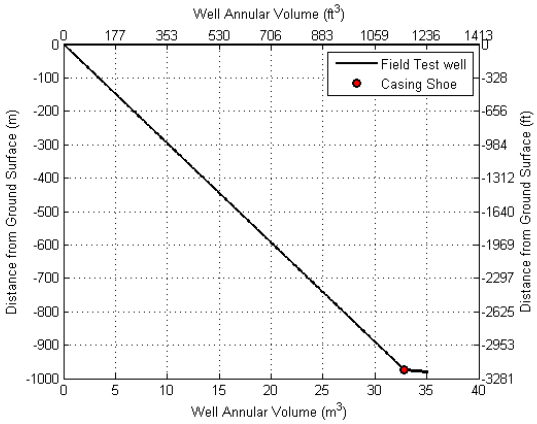

Figure 50 Annular volume of the Field Test well with respect to depth.

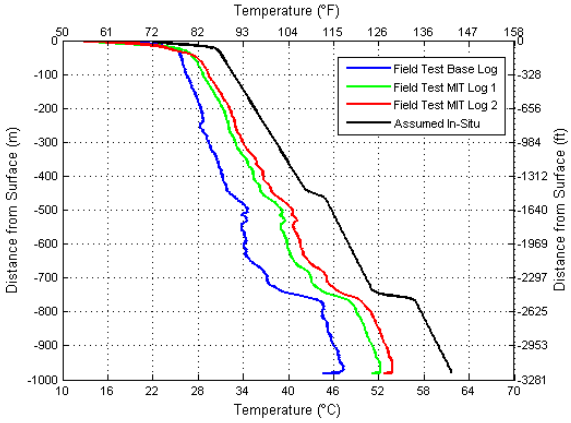

Figure 51 Assumed in-situ temperature distribution and temperature logs from the Field Test.

Table 14 Modeled sequence of events and corresponding time durations simulated during thermal analysis validation.

Event Description	Step Number	Event Duration (hours)	Cumulative Duration (hours)
Pre-Pressurization with Brine	I	15	15
Initial Stabilization Period	II	16	31
Initial N_2 Injection	III	1.5	32.5
Cemented Casing MIT	IV	0.75	33.25
Final N_2 Injection	V	0.5	33.75
Final Stabilization Period	VI	21	54.75
Casing Shoe MIT	VII	24	78.75

6.2 Results of Thermal Modeling Validation

The temperature distribution in the injection string of the Field Test well at the start and finish of the Field Test Casing Shoe MIT appear to be in good agreement with the modeled results of the Field Test. The temperature distributions from the Field Test temperature logs and the modeled values are shown in Figure 52. The error between the modeled and actual data was likely caused by a poor approximation of the assumed in-situ temperature distribution and a deviation between the actual and assumed material properties implemented into the modeling procedure.

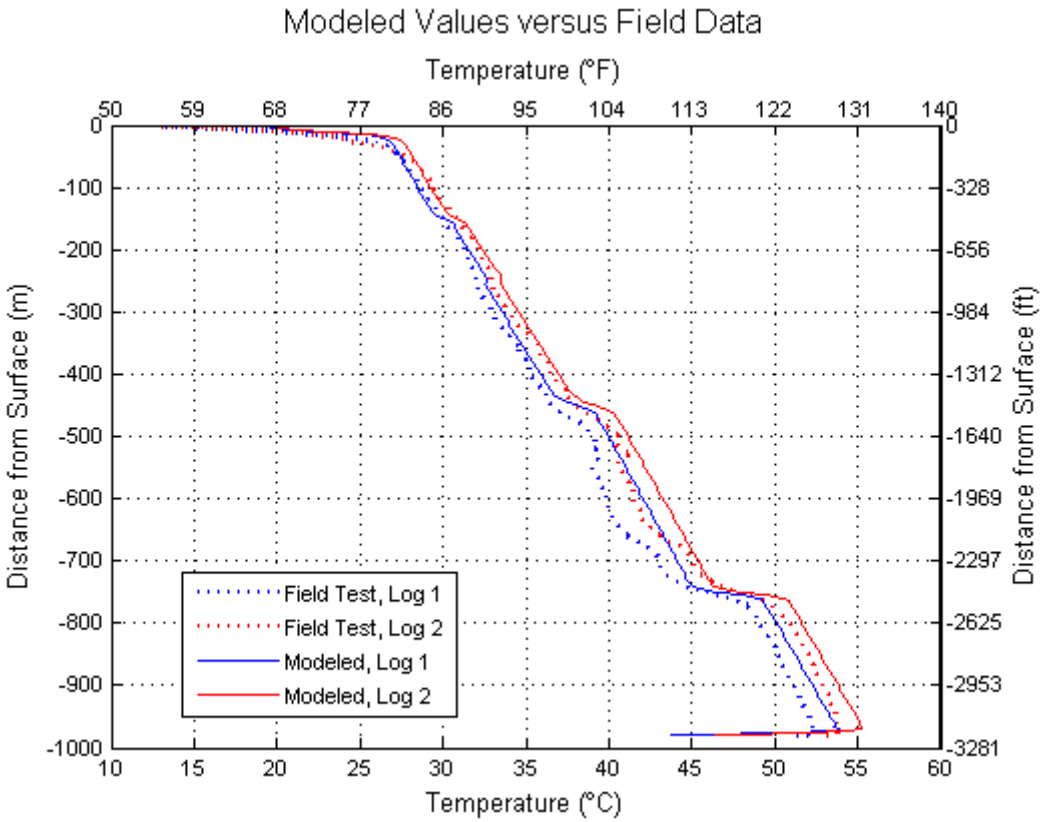

Figure 52 Field Test temperature logs and the corresponding modeled values of temperature distributions at the start and finish of the Field Test Casing Shoe MIT.

7 Nitrogen Volume Analysis

A volume analysis was performed by implementing the results of Steps VI and VII from the thermal modeling of the 18 scenarios. The analysis was performed by calculating the actual volume of nitrogen in the annulus; this was done using the initial temperature distribution in the annulus at the start of Step VI. An apparent volume of nitrogen in the annulus was calculated using the temperature distributions in the injection string of the thermal model. By comparing the actual and apparent volume calculations, the error between the apparent to actual values was determined. The relative change of the apparent volume of nitrogen with time was also calculated, and is referred to as the apparent leak rate. The actual leak rate simulated during this procedure was maintained at zero.

7.1 Constant Volume Calculation

A finite difference scheme was developed that implemented Equations 4 through 9 to calculate a constant incremental volume of nitrogen gas in the storage-well annulus, this was done by assuming (1) the nitrogen/brine interface depth was equal to that assumed during the thermal modeling, (2) the pressure gradient at the casing shoe was 0.018 MPa/m (0.8 psi/ft), and (3) the temperature distribution in the storage well annulus was equal to that computed by the thermal model. Using the temperature distribution in the annulus, as calculated from the thermal model, and assuming a constant incremental volume of nitrogen in the annulus with respect to time, the incremental change of pressure (also with respect to time) in the annulus was calculated using Equation 9 (Figure 53).

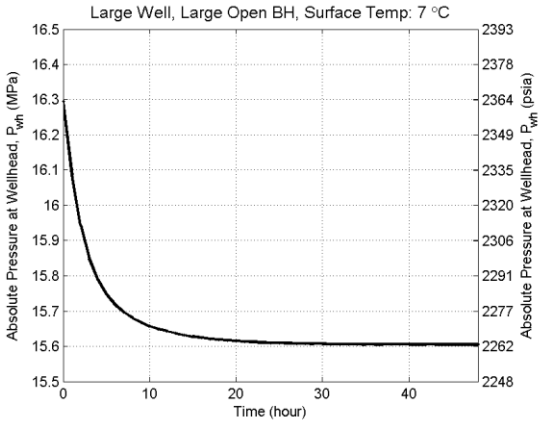

Figure 53 Analysis results of pressure on the nitrogen at the wellhead annulus of the Large well with a Large uncased borehole.

7.2 Apparent Volume Calculation

By implementing a similar scheme as was used for the constant volume calculation, an apparent volume calculation was made (Figure 54). The apparent volume calculations were made by implementing the following assumptions: (1) the nitrogen/brine interface depth was equal to that assumed during the thermal modeling, (2) the incremental pressure in the annulus was equal to the pressure resulting from the constant volume calculation, and (3) the temperature distribution in the injection string was equal to the temperature distribution determined from the thermal model. Also, the difference between the actual and apparent volume of nitrogen in the annulus was calculated with respect to time (Figure 55)

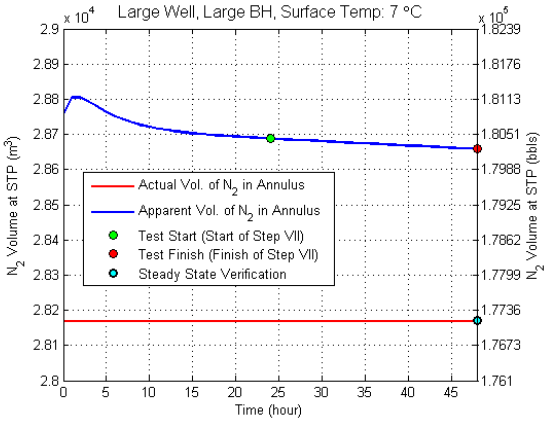

Figure 54 Actual and apparent volume calculations from the analysis of Step VII on the Large well with a Large uncased borehole.

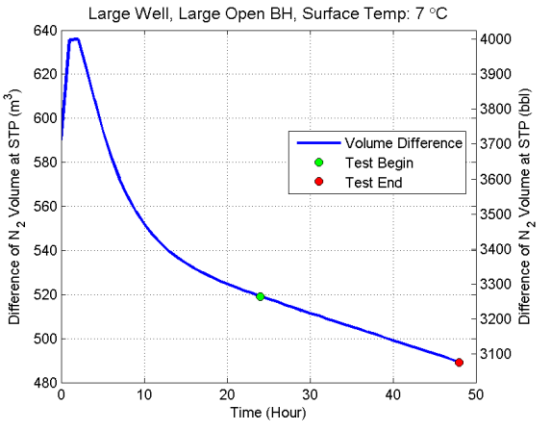

Figure 55 The difference of apparent and actual volume calculations from the analysis of Step VII on the Large well with a Large uncased borehole.

Theoretically, at some time after the final nitrogen injection, the temperature distribution in and around the storage well will reach steady state, at this time the temperature distribution in the annulus and injection string should be very nearly identical. When the temperatures in the injection string and annulus are nearly identical, the apparent volume and actual volume of nitrogen in the annulus should also be nearly identical. Through implementation of the thermal modeling results, calculated at steady-state, apparent and actual volumes of the nitrogen were calculated and used as a method of verification for the volume analysis.

The change of annular pressure at the wellhead associated with the all volume calculations are shown in Appendix E. An extended duration thermal model was also performed and the associated volume analysis, which shows the apparent volume calculation for a 240 hour (10 day) period beyond the start of Step VI, is shown in Appendix F.

8 Apparent Leak Rate Analysis

Apparent leak rates were calculated using the results from the volume analyses. The calculated apparent leak rates were based on a 24 hour period between volume measurements; as this is the industry standard for the duration of time between logging campaigns. The apparent leak rate, which is the relative change in the apparent volume, was calculated for each modeled scenario using the temperature and pressure at the casing shoe in the model; this was done in attempts to stay consistent with common testing practices. The temperature and pressure values, implemented for the apparent leak rate calculation, were observed in the injection string and annulus respectively.

8.1 Large Well

The apparent leak rates were calculated from the 48 and 240 hour volume analysis results and are illustrated in Figure 56 and Figure 57. The simulated surface temperature conditions were observed to have a large influence on the apparent leak rate calculations, as the rates corresponding to simulations with a 35 °C surface temperature were more than an order of magnitude less than those simulations performed with a surface temperature of 7 °C. The variations of the leak rate results calculated for the Large were correlated to similar variations observed in the sum of the temperature distribution (Appendix G.1). The maximum apparent leak calculated for the Large well was 268 m^3/year and the minimum was – 47 m^3/year (an apparent gain); both of these observed values occurred well before the standard 24 hour stabilization period. The maximum and minimum leak rates observed at the end of the standard 24 hour stabilization period were 67 and 0.6 m^3/year respectively, these were shown by calculations on the Large well with a Large uncased borehole modeled having a surface temperature of 7 °C and a Small uncased borehole modeled with a surface temperature of 35 °C.

The common trend observed from the apparent leak analysis of the Large wells, most notably when modeled with a 7 °C surface temperature, is the initial increase of the apparent leak rate shortly thereafter followed by a decrease. This trend was attributed to the annular temperature distribution initially warming at a much faster rate than the injection string followed by an increased rate in the warming of the injection string temperature distribution; this is illustrated in Figure 120, Figure 122, and Figure 124 of Appendix G.1.

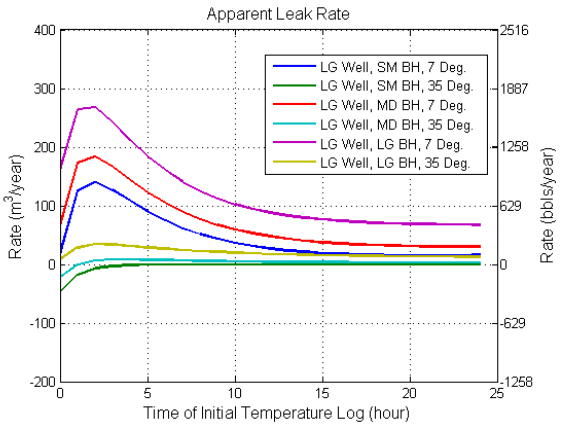

Figure 56 Apparent leak rates for a Large well with various uncased borehole dimensions and surface temperature conditions, over a 48 hour period.

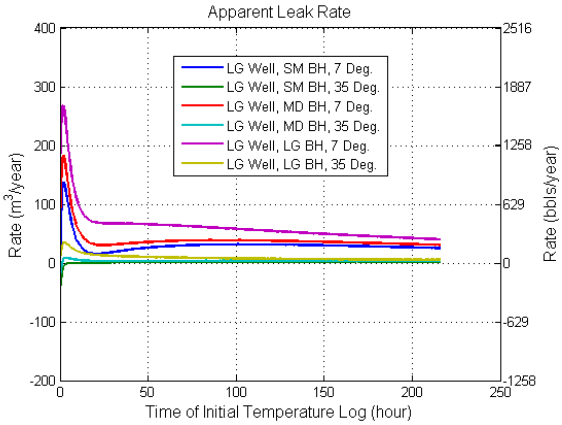

Figure 57 Apparent leak rates for a Large well with various uncased borehole dimensions and surface temperature conditions, over a 240 hour period.

8.2 Medium Well

The apparent leak rate results of the Medium well modeled for a 48 and 240 hour duration are shown in Figure 58 and Figure 59. The results from the Medium well fall within a much closer range than those calculated from the large well; the maximum and minimum apparent leak rate values were 11 and – 7 m^3/year respectively, with both of these values occurring at the start of the stabilization period. The maximum and minimum observed values at the end of the standard 24 stabilization periods were 7 m^3/year from the Medium well with a Large uncased borehole modeled with a 7 °C surface temperature and -1 m^3/year from the Medium well with a Small uncased borehole modeled having 35 °C surface temperature.

The apparent leak rate trends for the Medium well appear to be separated into a dichotomy dependent on the simulated surface temperature conditions. Wells modeled with 35 °C surface temperatures have a relatively smaller apparent leak rate and less variability of the leak rate than wells modeled with 7 °C surface temperatures.

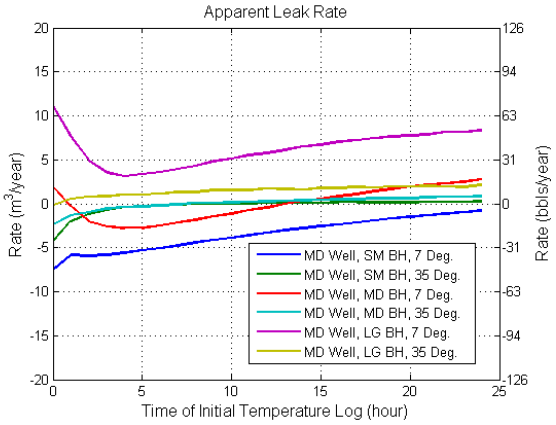

Figure 58 Apparent leak rates for a Medium well with various uncased borehole dimensions and surface temperature conditions, over a 48 hour period.

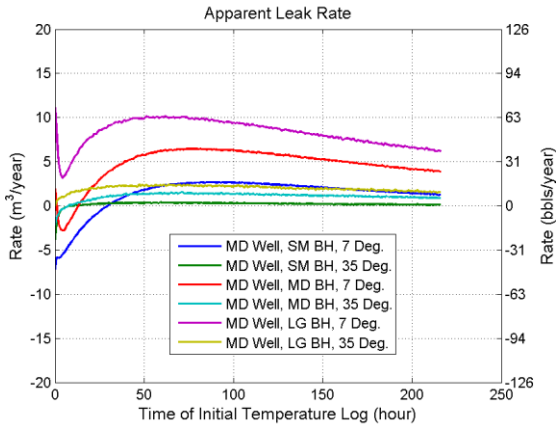

Figure 59 Apparent leak rates for a Medium well with various uncased borehole dimensions and surface temperature conditions, over a 240 hour period.

8.3 Small Well

The apparent leak rate results of the Small well modeled for a 48 and 240 hour duration are shown in Figure 60 and Figure 61. The maximum and minimum apparent leak rate values were 8 and – 3 m³/year. The maximum and minimum apparent leak rates were observed at a time of 48 and 2 hours from the start of the initial stabilization period.

The apparent leak rate results from the Small well are similar in booth size and magnitude to those of the Medium well. The reason for the similarities of apparent leak rates may be traced back to the similar annular and injection string temperature distributions at the start of the stabilization period (Appendix G.2 and G.3)

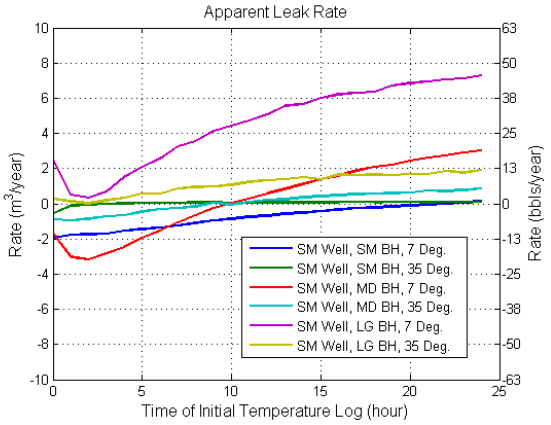

Figure 60 Apparent leak rates for a Small well with various uncased borehole dimensions and surface temperature conditions, over a 48 hour period.

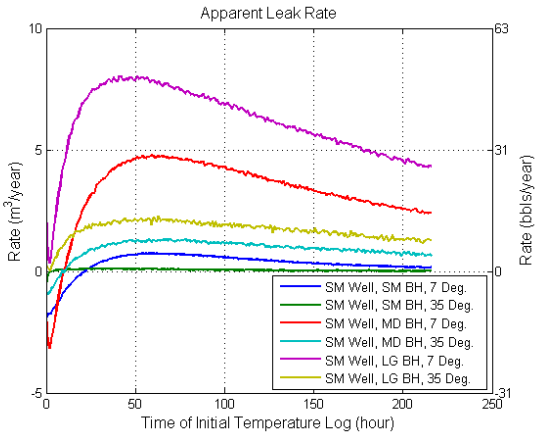

Figure 61 Apparent leak rates for a Small well with various uncased borehole dimensions and surface temperature conditions, over a 240 hour period.

8.4 Influence of Surface Conditions

Apparent leak results from all models simulated with surface temperatures of 7 °C have been illustrated in Figure 62 and adjacently Figure 63 shows all but the Large wells simulated with the same surface conditions. Apparent leak rate results from all models simulated having a 35 °C surface temperature are shown in Figure 64, while Figure 65 includes all models except for the Large wells simulated having the same surface conditions.

The apparent leak rate values calculated for the Large well with a 7 °C surface condition are much greater than all other values; this was caused by the much larger initial variation between the annular and injection string temperature (Appendix G.1) and the significantly greater well volume (Appendix C.1).

All wells, regardless of size, were calculated as having an apparent leak rate closer to zero when simulated with the warmer (35 °C) surface condition. The maximum and minimum values calculated from the Small and Medium wells with a 35 °C surface temperature were 2.5 and -4 m^3/day, while the maximum and minimum values calculated from the same wells but with a modeled 7 °C surface temperature were 10 and -7 m^3/day.

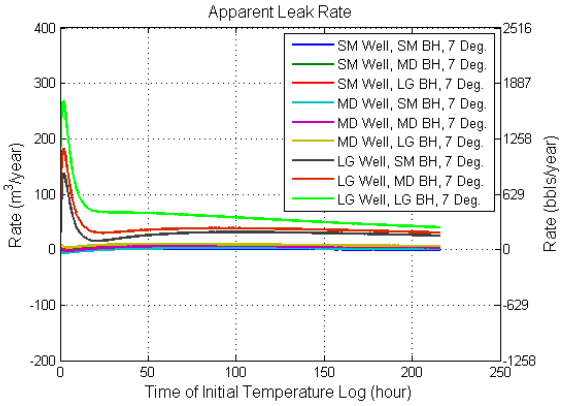

Figure 62 Apparent leak rates for all wells modeled with 7 °C surface conditions.

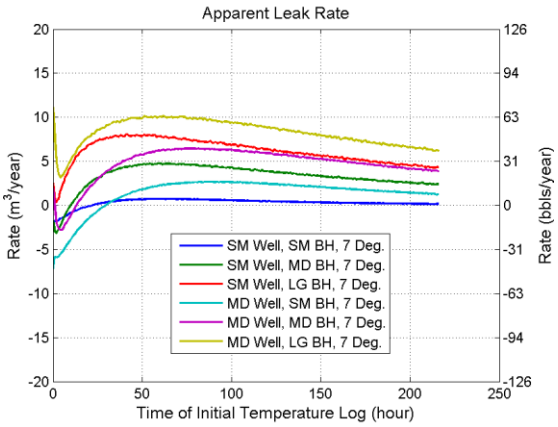

Figure 63 Apparent leak rates for wells modeled with 7 °C surface conditions (excluded Large wells).

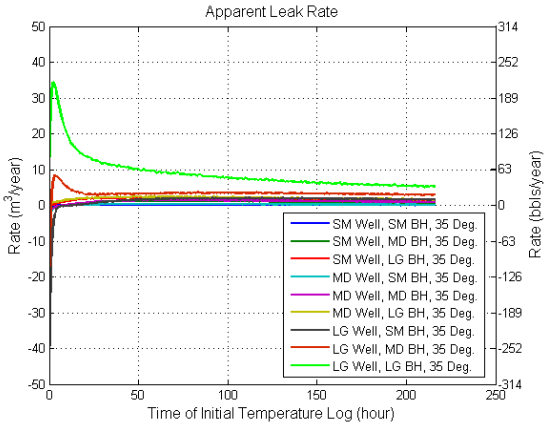

Figure 64 Apparent leak rates for all wells modeled with 35 °C surface conditions.

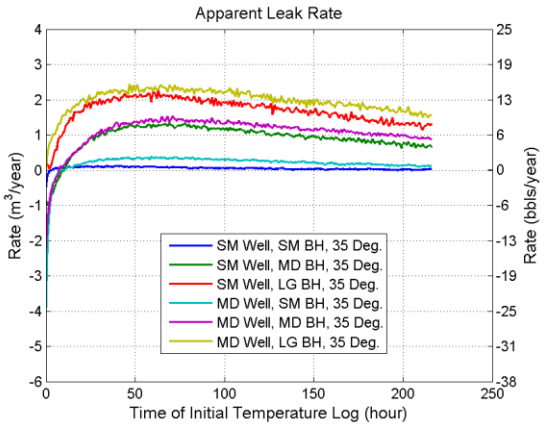

Figure 65 Apparent leak rates for wells modeled with 35 °C surface conditions (excluded Large wells).

The absolute value of the calculated apparent leak rate for all well sizes simulated with both surface temperatures (7 and 35 °C) are shown with a 24 hour final stabilization period (Figure 66) and a 216 hour final stabilization period (Figure 67). Absolute apparent leak rate values were greater (farther from the actual leak rate of zero) in wells simulated with having a cooler, 7 °C, surface temperature after a 24 and 216 hour final stabilization period than in wells simulated with a warmer, 35 °C, surface temperature.

The cause for the increased values of absolute apparent leak rates in wells simulated having a 7 °C surface temperature is (1) the injection temperature of the brine during prepressurization will be colder and create a greater difference between the injection string and the in-situ

temperature distributions and (2) the temperature that nitrogen is injected at, which is the calculated linear temperature average in the injection string, will be colder and thus require a greater temperature change to reach steady state. These two causes result in the injection string and annular temperature distributions requiring a greater time period to reach steady state and the volume of nitrogen requiring a greater change between the initial injection volume and the steady – state volume; each of these resulting in larger error of the calculated apparent leak rate.

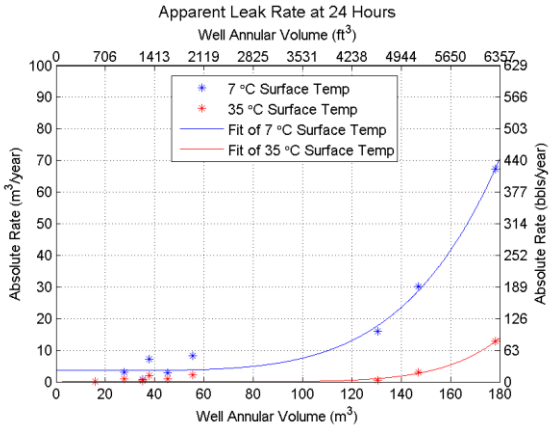

Figure 66 Comparison of absolute apparent leak rates for all well sizes with a 24 hour stabilization period.

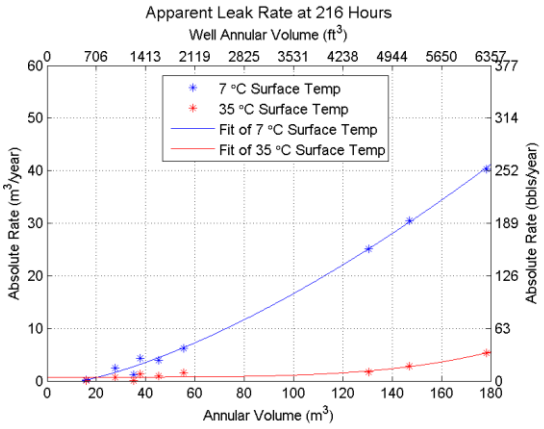

Figure 67 Comparison of absolute apparent leak rates for all well sizes with a 216 hour (9 day) stabilization period.

9 Conclusions

The objectives of this research were to more thoroughly understand how and to what extent the variation of the time between the beginning of the final stabilization period (Step VI) and the start of the Casing Shoe MIT (Step VII), well geometry, and surface conditions during a NBT influence the calculated apparent leak rate results. The objectives of this research were accomplished through finite element modeling of the thermal phenomena associated with the NBT on an array of idealized storage-well geometries having surface temperatures of 7 and 35 °C. The thermal modeling results were then implemented into an apparent leak rate analysis that calculated the nature and magnitude of the corresponding apparent leak rate.

The conducted research revealed that well volume (a function of the well and uncased borehole sizes) and surface temperature conditions have a significant influence on both the magnitude and nature of the apparent leak rate. The well volume influences the nature (i.e. either positive or negative) of the apparent leak rate by creating a reduced thermal gradient between the injection string and the adjacent strata, which slows the rate of conductive heat transfer; the well volume also influences the magnitude of the apparent leak by defining the volume of nitrogen stored in the annulus.

Other observed conclusions were:

- All wells modeled with the colder (7 °C) surface temperature consistently had apparent leak rates that deviated farther from the actual leak rate, which was zero, than the same wells when modeled with the warmer (35 °C) surface temperature.
- All wells modeled with a Small uncased borehole had a significantly more accurate apparent leak rate results than when modeled with a Medium or Large uncased borehole.
- As the modeled well volume decreased, simulations modeled with 7 °C surface temperatures showed more sustained negative apparent leak rates (i.e. an apparent gain of nitrogen volume).
- More accurate test results may be obtained by injecting nitrogen gas that more closely represents the temperature in the injection string; this may be done by injecting nitrogen at the volumetric temperature average rather than the linear temperature average.

10 References

Bérest, P., B. Brouard, and G. Durup. "Tightness Tests in Salt-Cavern Wells." *Oil & Gas Science and Technology* (Éditions Technip) 56 (2001): 451-469.

Crotogino, Fritz. "SMRI References for External Well Mechanical Integrity Testing / Performance, Data Evaluation and Assessment." Solution Mining Research Institute Research Project Report 95-0001-S, Kavernen Bau- und Betriebs-GmbH (KBB), 1995, 62.

Cengel, Yunus A., and M. A. Boles. "Thermodynamics: An Engineering Approach – 5th Edition." McGraw Hill – Higher Eduation. Boston. MA. 2006. 988.

Dittman, Gerald L. "Calculation of Brine Properties." Lawerence Livermore Laboratory Formal Report. UCID – 17406. 1977. 26.

Djahanguiri, F., and S. C. Matthews. "Geotechnical Considerations for Design of a Nuclear Repository in Bedded Salt in the U.S." *Sixth International Symposium on Salt.* Salt Institute, 1983. 24.

Evans, David J. "Accidents at Underground Fuel Storage Sites and Risk Relative to Other Areas of the Energy Supply Chain, with Particular Reference to Salt Cavern Storage." *SMRI Fall 2008 Technical Conference.* Galveston, TX, 2008. 19.

Gatelier, N., T. You, P. Bérest, and B. Brouard. "Adiabatic Temperature Changes in an Oil-Filled Cavern." *SMRI Fall 2008.* Galveston, TX, 2008. 23.

Gresho, P. M., and R. L. Sani. "Incompressible Flow and the Finite Element Method: Advection – Diffusion and Isothermal Laminar Flow." John Wilely and Sons. New York, NY. 1998. 1021.

Heitmann, Norbert A. "Experience with Cavern Integrity Testing using Nitrogen Gas." *SMRI Spring 1987Meeting Paper.* Tulsa, OK, 1987. 34.

Kansas Department of Health and Environment (KDHE). "Nitrogne/Brine Interface Mechanical Integrity Test (MIT)." Bureau of Water – Geology Section. Topeka, KS. Procedure#: UICLPG-18. 2005. 10.

Kelsall, Peter C., and Jeffrey W. Nelson. "Geologic and Engineering Characteristics of Gulf Region Salt Domes Applied to Underground Storage and Mining." Sixth International Symposium on Salt, Volume 1. 1983. 26.

Meter, Donald M., R.B. Bird. "Turbulent Newtonian Flow in Annuli." American Institute of Chemical Engineering Journal. Volume 7. Issue 1. 1961. 41-45.

Nelson, Paul E., and Leo L. Van Sambeek. "State-of-the-Art Review and New Techniques for Mechanical Integrity Tests of (Gas-Filled) Natural Gas Storage Caverns." SMRI Research Project Report 2003-2, 2003. 92.

National Oceanic and Atmosphere Administration (NOAA). “Monthly Weather Summary.” Houston/Galveston Weather Forecast Office. Obtained February 2, 2011 from the World Wide Web at: http://www.weather.gov/climate/index.php?wfo=hgx.

National Institute of Standards and Tchnology (NIST), 2010. NIST Standard Reference Fluid Properties Database 23 (miniREFPROP): Version 9.0. Obtained February 1, 2011 from World Wide Web at: http://www.boulder.nist.gov/div838/theory/refprop/MINIREF/MINIREF.HTM.

NOWSCO Technical Manual, Section II, “Basis of calculations used in graphs, charts, and tables.” NOWSCO Services. 1980

Ratigan, Joe L., and R. Blair. “Temperature Logging in Drillholes in Domal Salt.” *SMRI Fall 1994 Meeting Paper*. Hannover, Germany, 1994. 19.

Sage, Bruce H., and W. N. Lacey. “Thermodynamic Properties of the Lighter Paraffin Hydrocarbons and Nitrogen.” Reproduced In: NOWSCO Technical Manual, Section II. 1980. Published by: American Petroleum Institute. New York. NY. 1950

Southern Methodist University (SMU) Geothermal Laboratory. “Western Geothermal Area Database.” Obtained February 15, 2011. From the World Wide Web at: http://smu.edu/geothermal/georesou/s_centrl.htm.

Svalstad, D. K. “Documentation of Spectrom-45: A Finite Element Heat Transfer Analysis Program; Revision 0.” Report Numbers: DOE/CH/10378-1; SAND--88-7122; RSI--0269-1; RSI--0266-1. Research Organization: RE/SPEC, Inc., Rapid City, SD, 1989. 872.

Thoms, R. L., and R. M. Gehle. “Survey of Existing Caverns in U.S. Salt Domes.” SMRI Research Project Report 84-0002, 1984. 47.

Van Sambeek, L., P. Bérest, and B. Brouard, "Improvements in Mechanical Integrity Tests for Solution-Mined Caverns Used for Mineral Production or Liquid-Product Storage." Solution Mining Research Institute Research Report 2005-1, 2005. 142.

Weidman, P. D., and G. Mehrdadtehrarnfar. “Instability of Natural Convcetion in a Tall Vertial Annulus.” Dept. of Mech. Engineering, Univ. of Colorado, Boulder. Journal: Physics of Fluids. Volume 28. March, 1985. 776 – 787.

Appendix A: Assumption of Natural Convection

The onset of natural convection (buoyancy driven flow) is characterized by the dimensionless Rayleigh number (Ra). When the Rayleigh number is below a calculated critical value, heat transfer occurs dominantly in the form of conduction, and when the Rayleigh number is greater than the critical value the dominate heat transfer mode is natural convection. The equation for the Rayleigh number, which is the product of the Grashof and Prandtl numbers, is:

(Equation 10)

$$\mathrm{Ra} = \frac{g\beta\Delta T L^3}{\nu D}$$

where:

Ra (r,z)	=	Rayleigh number at position (r,z)
g	=	constant of gravitational acceleration
β	=	coefficient of expansivity
ν	=	kinematic viscosity
D	=	thermal diffusivity
ΔT	=	temperature contrast between walls
L	=	gap width in annulus

For annular enclosures, the critical Rayleigh number is [Weidman & Mehrdadtehrarnfar, 1985]:

(Equation 12)

$$\mathrm{Ra_{cr}} = 300\frac{H}{L}$$

where:

Ra_{cr}	=	critical Rayleigh number
H	=	gap height in annulus
L	=	gap width in annulus

Using parameter values that were consistent with this research a maximum Ra value of approximately 300 and a Ra_{cr} of 8×10^6 was calculated using the temperature values at the casing shoe. Because the maximum value of Ra was much less than the Ra_{cr}, the influence of natural convection on the thermal modeling was neglected. This assumption is also reinforced by the observation of an appreciable temperature gradient with depth as observed in the Field Test temperature logs; this gradient would not be nearly as prevalent if natural convection was the dominant mode of heat transfer in the annulus.

Appendix B: Calculation of Compressibility Factor (Z)

To allow for computer application, the compressibility factor (Z) is fit to a curve over three pressure ranges in the form of:

$$Z = AP^2 + BP + C$$

The constants A, B, and C were then made to fit the correct curve over a give pressure range. The results are as follows:

For: $500 < P < 4000$

$A = 1.679393\times10^{-7} - 6.2243\times10^{-10}\,T + 8.0385\times10^{-13}T^2 - 3.5472\times10^{-16}T^2$

$B = -3.122\times10^{-4} + 8.488\times10^{-7}T - 5.37\times10^{-10}T^2$

$C = 1.0$

For: $4000 < P < 8000$

$A = 0$

$B = 2.2817\times10^{-4} - 4.066\times10^{-7}T + 2.3\times10^{-10}T^2$

$C = -0.0956 + 2.5\times10^{-3}T - 1.5\times10^{-6}T^2$

For: $P > 8000$

$A = 0$

$B = 2.2042\times10^{-4} - 3.515\times10^{-7}T + 1.815\times10^{-10}T^2$

$C = -0.1573 + 2.438\times10^{-3}T - 1.4\times10^{-6}T^2$

P = pressure (psi)

T = temperature (R)

These data resulted in accuracy over the entire range of ±1%

These data were obtained from: NOWSCO Technical Manual, 1980 and Bruce & Sage, 1950

Appendix C: Storage Well Volumes

The volume in the storage well consists of two distinct areas: (1) annulus between the cemented casing and injection string that is above the casing shoe and (2) volume between the outer diameter of the uncased borehole and the injection string that is below the casing show and above the cavern roof. The volume of all modeled storage wells included in this research will be illustrated herein.

C.1 Large Well

Volumes of the Large well with different uncased borehole sizes are shown in Figure 68 through Figure 70.

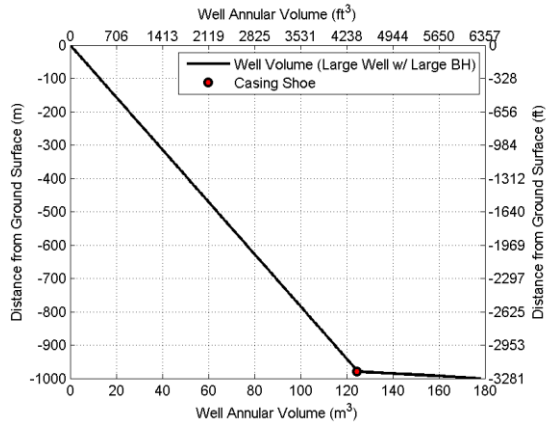

Figure 68 Volume of Large well with a Large uncased borehole.

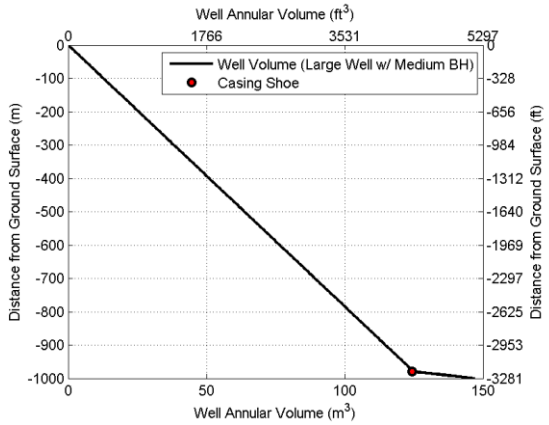

Figure 69 Volume of Large well with a Medium uncased borehole.

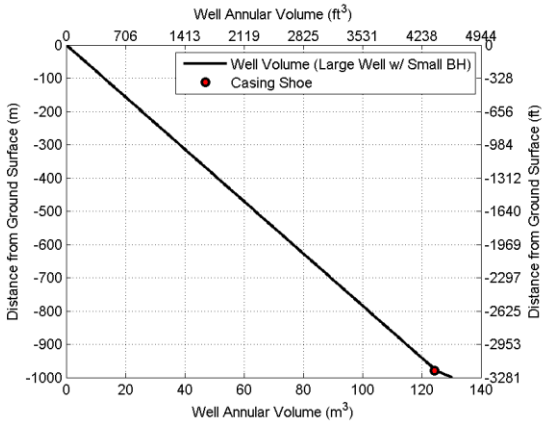

Figure 70 Volume of Large well with a Small uncased borehole.

C.2 Medium Well

Volumes of the Medium well with different uncased borehole sizes are shown in Figure 71 through Figure 73.

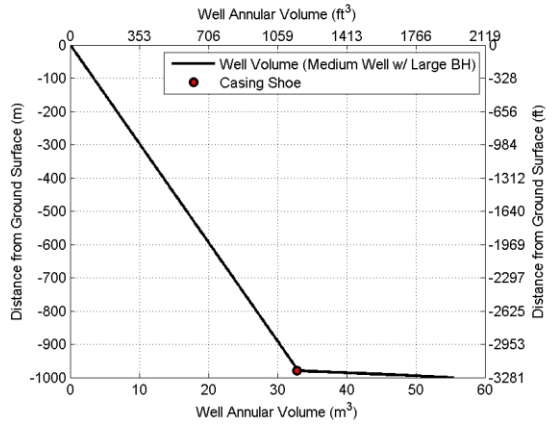

Figure 71 Volume of Medium well with a Large uncased borehole.

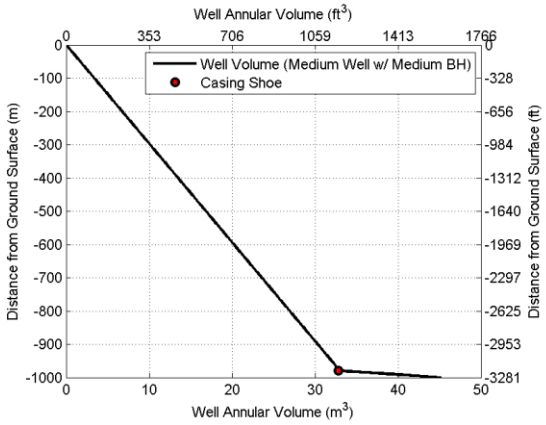

Figure 72 Volume of Medium well with a Medium uncased borehole.

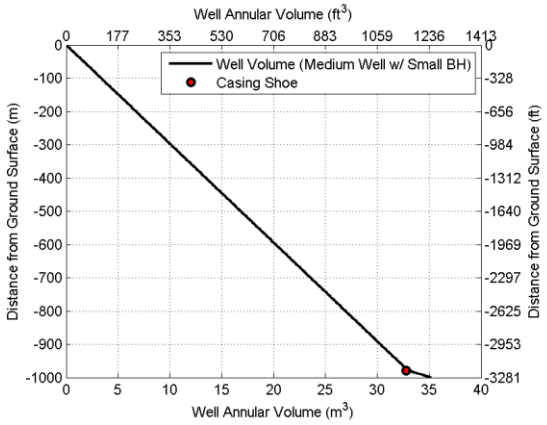

Figure 73 Volume of Medium well with a Large uncased borehole.

C.3 Small Well

Volumes of the Medium well with different uncased borehole sizes are shown in Figure 74 through Figure 76.

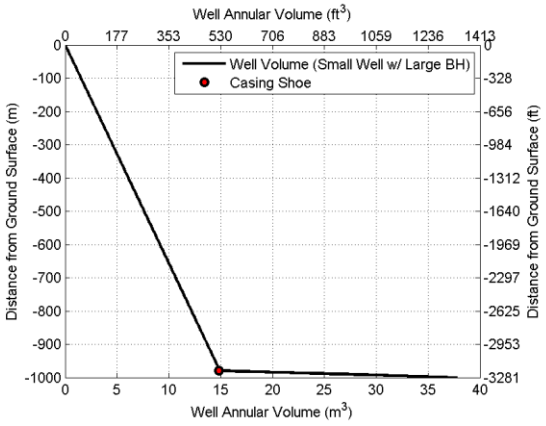

Figure 74 Volume of Small well with a Large uncased borehole.

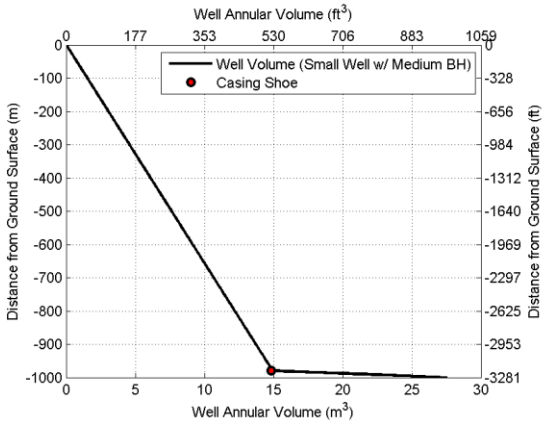

Figure 75 Volume of Small well with a Medium uncased borehole.

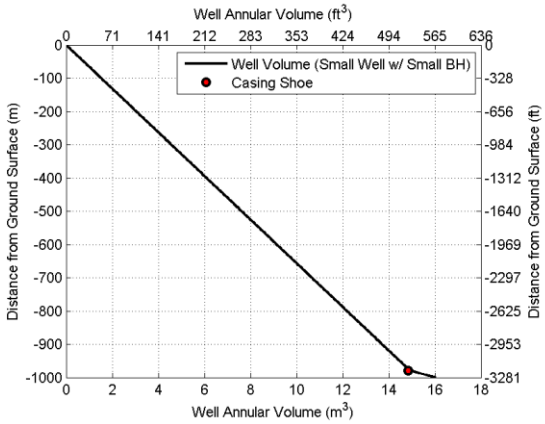

Figure 76 Volume of Small well with a Large uncased borehole.

Appendix D: Variability of N_2 Properties

The thermophysical properties of nitrogen change noticeable with varying values of temperature and pressure. The modeled thermophysical property value for nitrogen and typical upper and lower limits of values encountered during a NBT are illustrated for specific heat at constant pressure (Figure 77), density (Figure 78), Prandtl number (Figure 79), thermal conductivity (Figure 80), thermal diffusivity (Figure 81), and viscosity (Figure 82).

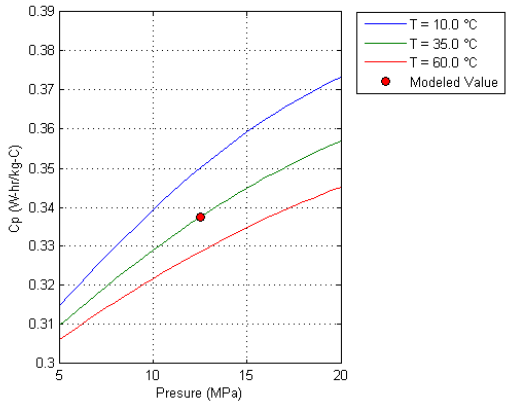

Figure 77 The Variation of specific heat (Cp) with temperature and pressure.

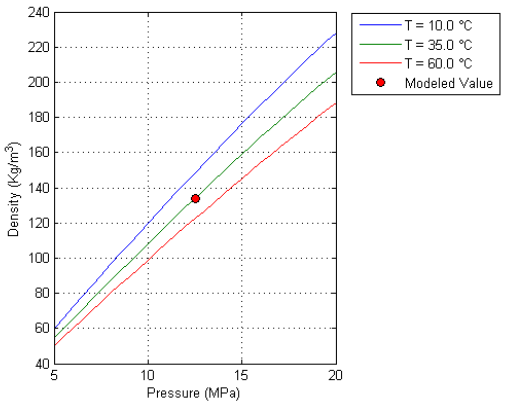

Figure 78 The Variation of density with temperature and pressure.

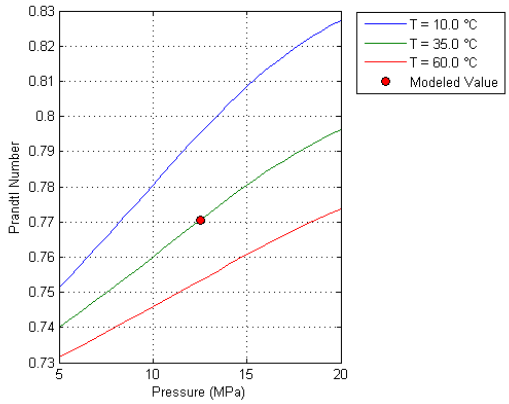

Figure 79 The Variation of Prandtl number with temperature and pressure.

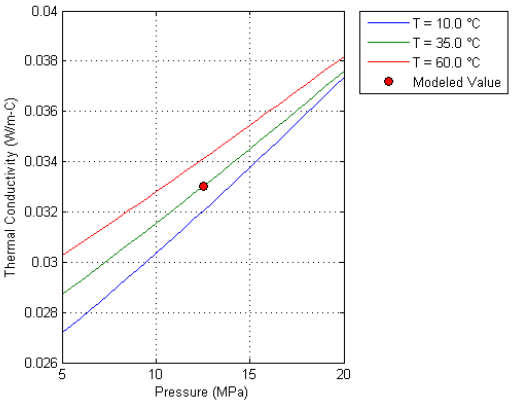

Figure 80 The Variation of thermal conductivity with temperature and pressure.

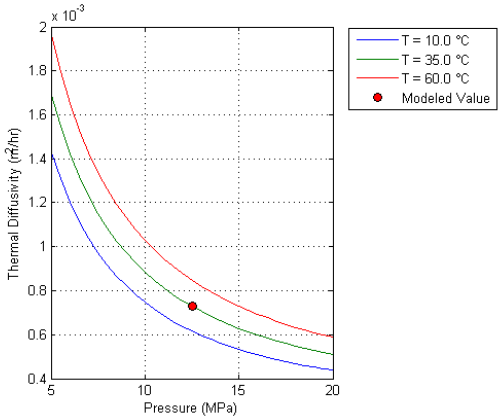

Figure 81 The Variation of thermal diffusivity with temperature and pressure.

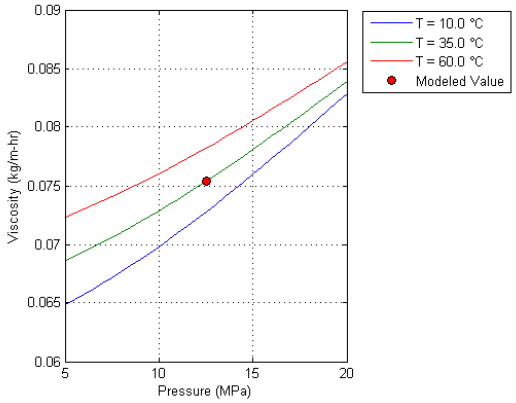

Figure 82 The Variation of viscosity with temperature and pressure.

Appendix E: Wellhead Annular Pressure during a NBT

The following pressure versus time values were calculated during the volume analysis portion of this research project.

E.1 Large Well

The wellhead annular pressure results for the Large well (Figure 83 through Figure 88) modeled with three different uncased borehole (BH) sizes and two different brine surface temperatures are shown:

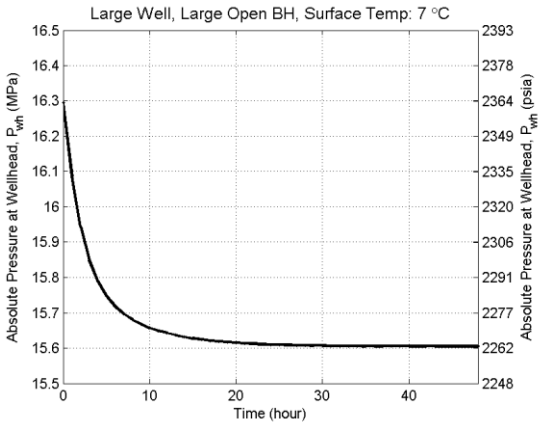

Figure 83 Nitrogen pressure at the wellhead annulus calculated during the volume analysis of the Large well with a Large uncased borehole simulated with a surface temperature of 7 °C.

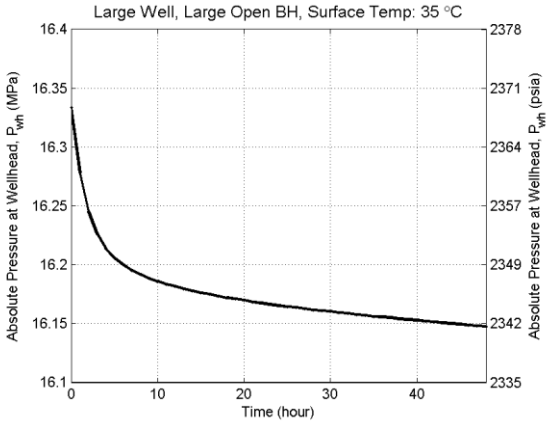

Figure 84 Nitrogen pressure at the wellhead annulus calculated during the volume analysis of the Large well with a Large uncased borehole simulated with a surface temperature of 35 °C.

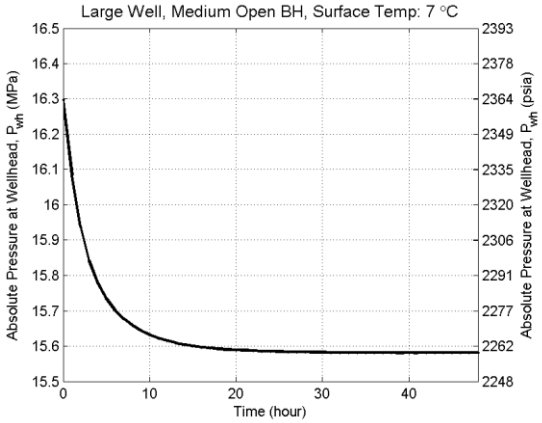

Figure 85 Nitrogen pressure at the wellhead annulus calculated during the volume analysis of the Large well with a Medium uncased borehole simulated with a surface temperature of 7 °C.

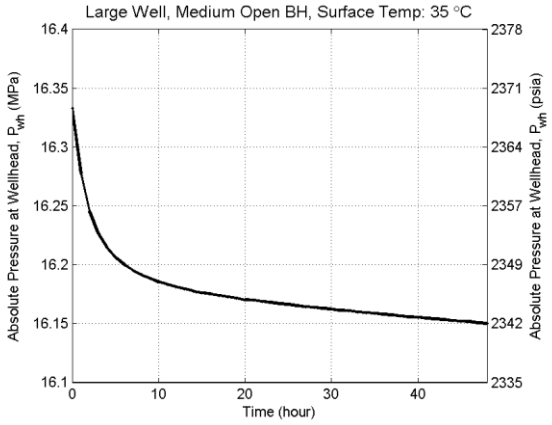

Figure 86 Nitrogen pressure at the wellhead annulus calculated during the volume analysis of the Large well with a Medium uncased borehole simulated with a surface temperature of 35 °C.

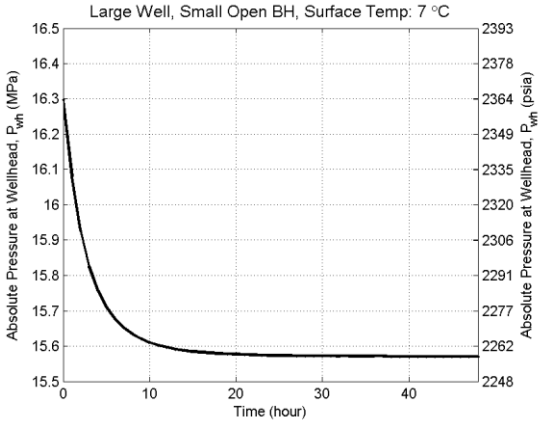

Figure 87 Nitrogen pressure at the wellhead annulus calculated during the volume analysis of the Large well with a Small uncased borehole simulated with a surface temperature of 7 °C.

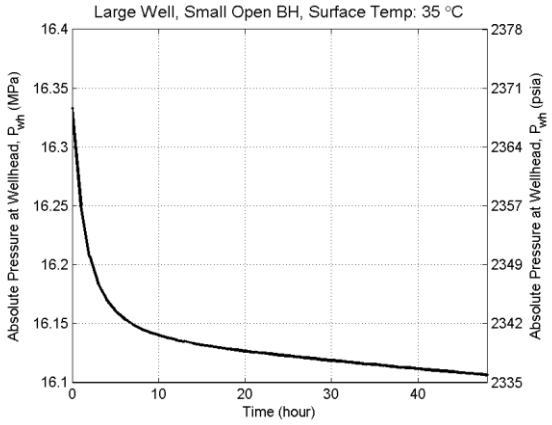

Figure 88 Nitrogen pressure at the wellhead annulus calculated during the volume analysis of the Large well with a Small uncased borehole simulated with a surface temperature of 35 °C.

E.2 Medium Well

The wellhead annular pressure results for the Medium well (Figure 89Figure 83 through Figure 94) modeled with three different uncased borehole (BH) sizes and two different brine surface temperatures are shown:

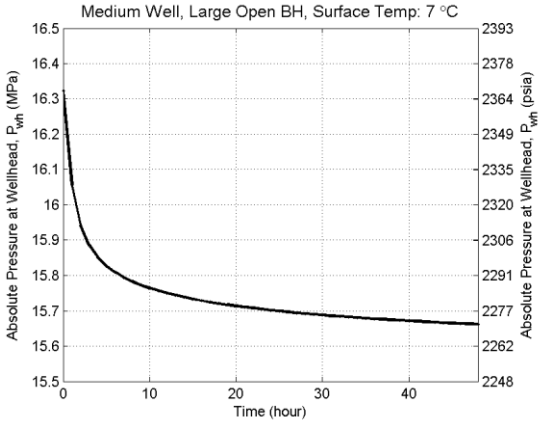

Figure 89 Nitrogen pressure at the wellhead annulus calculated during the volume analysis of the Medium well with a Large uncased borehole simulated with a surface temperature of 7 °C.

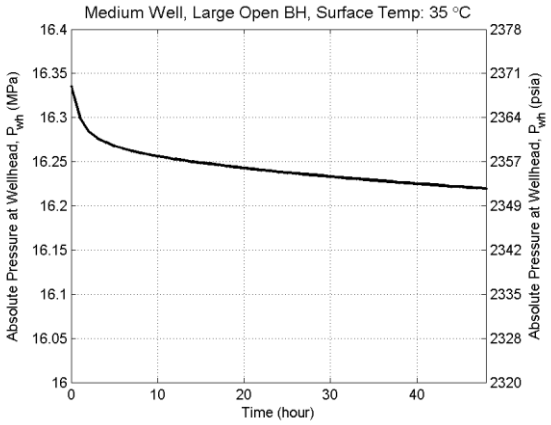

Figure 90 Nitrogen pressure at the wellhead annulus calculated during the volume analysis of the Medium well with a Large uncased borehole simulated with a surface temperature of 35 °C.

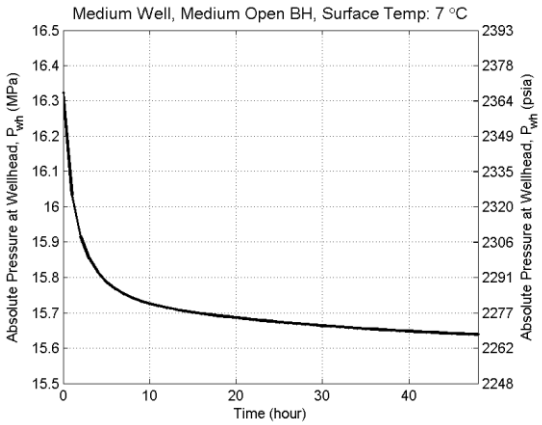

Figure 91 Nitrogen pressure at the wellhead annulus calculated during the volume analysis of the Medium well with a Medium uncased borehole simulated with a surface temperature of 7 °C.

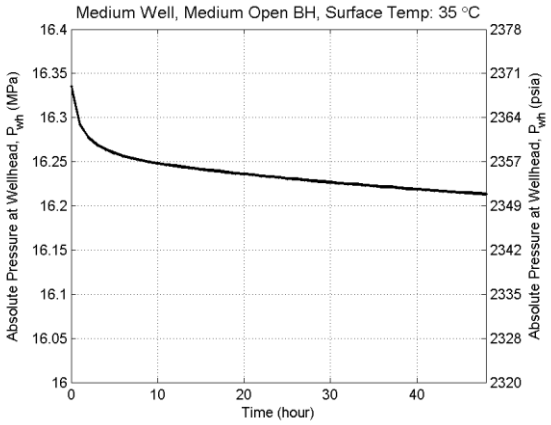

Figure 92 Nitrogen pressure at the wellhead annulus calculated during the volume analysis of the Medium well with a Medium uncased borehole simulated with a surface temperature of 35 °C.

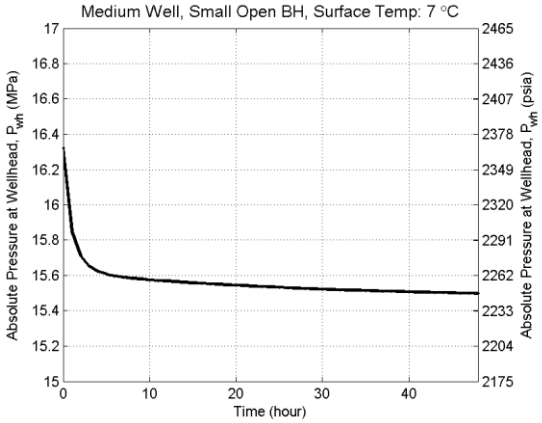

Figure 93 Nitrogen pressure at the wellhead annulus calculated during the volume analysis of the Medium well with a Small uncased borehole simulated with a surface temperature of 7 °C.

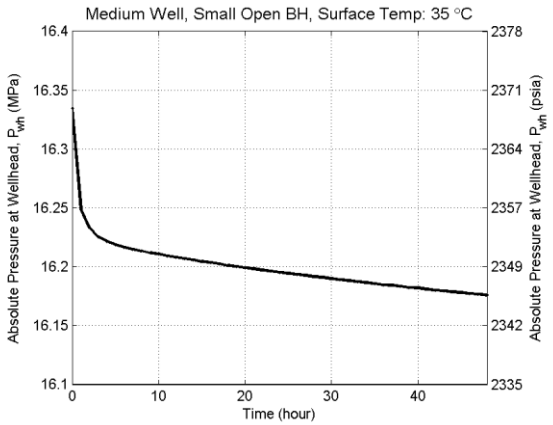

Figure 94 Nitrogen pressure at the wellhead annulus calculated during the volume analysis of the Medium well with a Small uncased borehole simulated with a surface temperature of 35 °C.

E.3 Small Well

The wellhead annular pressure results for the Small well (Figure 95Figure 83 through Figure 100) modeled with three different uncased borehole (BH) sizes and two different brine surface temperatures are shown:

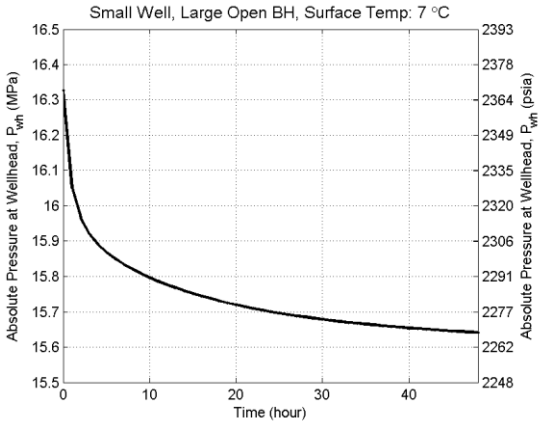

Figure 95 Nitrogen pressure at the wellhead annulus calculated during the volume analysis of the Small well with a Large uncased borehole simulated with a surface temperature of 7 °C.

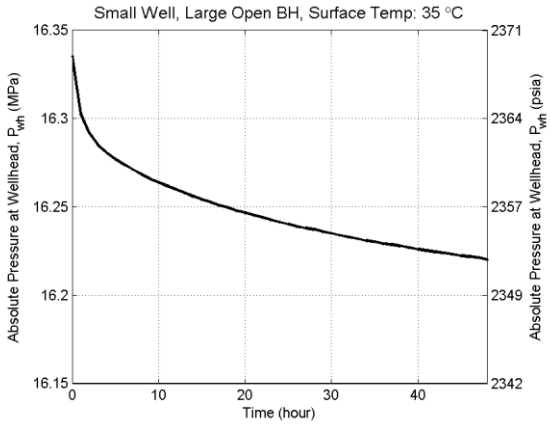

Figure 96 Nitrogen pressure at the wellhead annulus calculated during the volume analysis of the Small well with a Large uncased borehole simulated with a surface temperature of 35 °C.

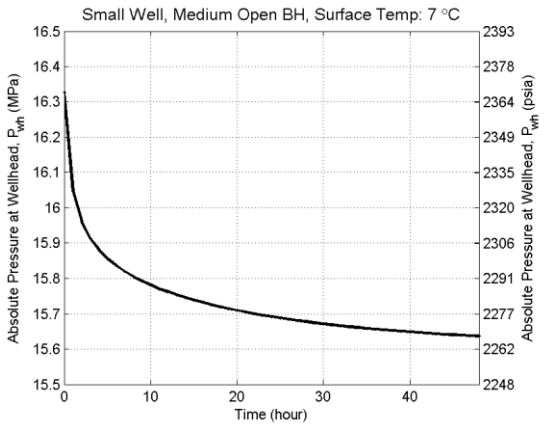

Figure 97 Nitrogen pressure at the wellhead annulus calculated during the volume analysis of the Small well with a Medium uncased borehole simulated with a surface temperature of 7 °C.

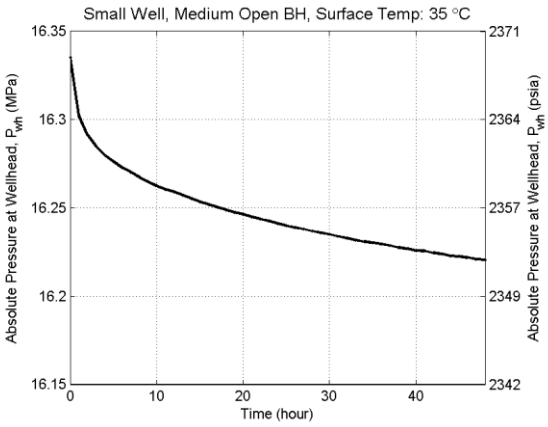

Figure 98 Nitrogen pressure at the wellhead annulus calculated during the volume analysis of the Small well with a Medium uncased borehole simulated with a surface temperature of 35 °C.

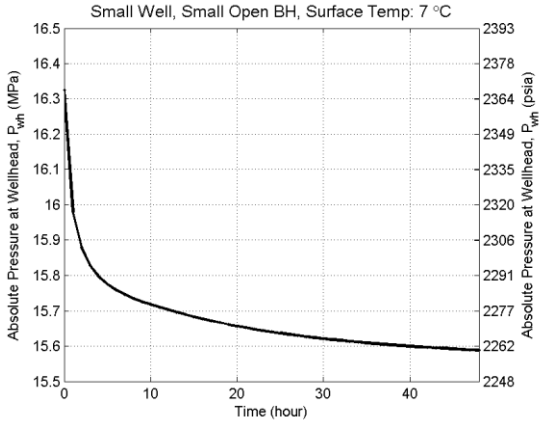

Figure 99 Nitrogen pressure at the wellhead annulus calculated during the volume analysis of the Small well with a Small uncased borehole simulated with a surface temperature of 7 °C.

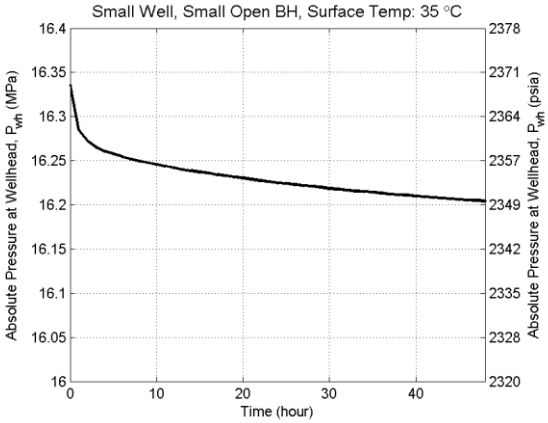

Figure 100 Nitrogen pressure at the wellhead annulus calculated during the volume analysis of the Small well with a Small uncased borehole simulated with a surface temperature of 35 °C.

Appendix F: Extended Duration Volume Analysis

The results shown below are similar to that discussed in the 'Volume Analysis' section but with an extended duration of 240 hours (10 days) instead of only 48 hours which were previously displayed.

F.1 Large Well

The modeled actual and apparent volume results for the Large well (through) modeled with three different uncased borehole (BH) sizes and two different brine surface temperatures are shown:

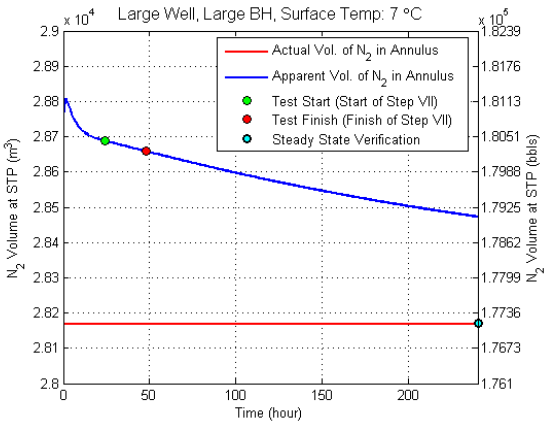

Figure 101 Actual and apparent volume calculations at STP for the Large well with Large uncased borehole modeled with a surface temperature of 7 °C.

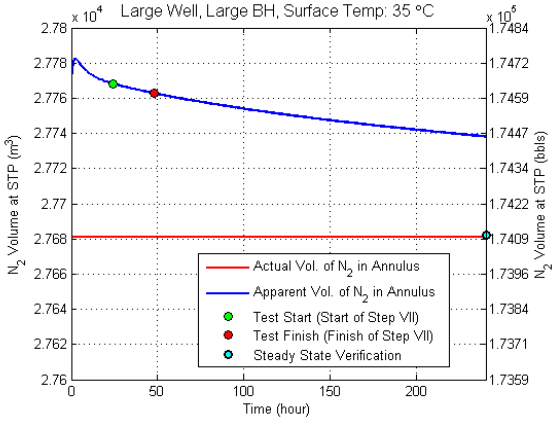

Figure 102 Actual and apparent volume calculations at STP for the Large well with Large uncased borehole modeled with a surface temperature of 35 °C.

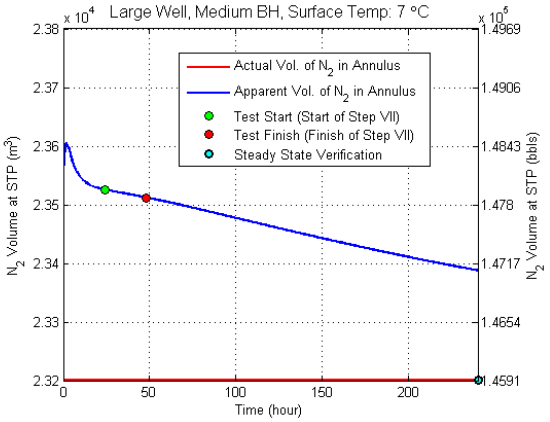

Figure 103 Actual and apparent volume calculations at STP for the Large well with Medium uncased borehole modeled with a surface temperature of 7 °C.

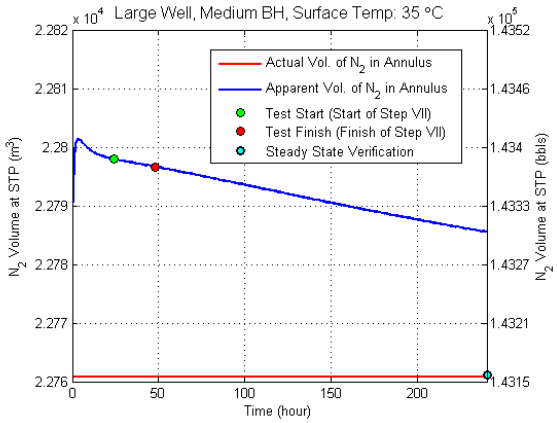

Figure 104 Actual and apparent volume calculations at STP for the Large well with Medium uncased borehole modeled with a surface temperature of 35 °C.

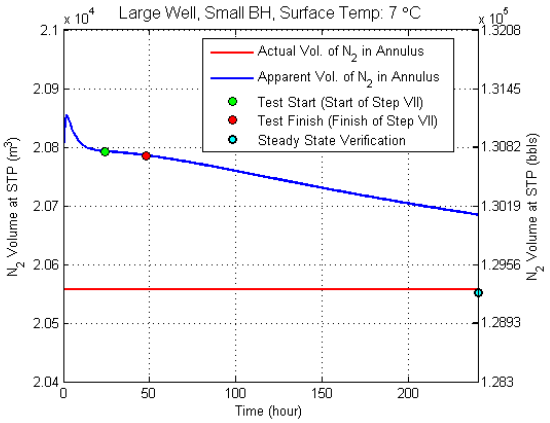

Figure 105 Actual and apparent volume calculations at STP for the Large well with Small uncased borehole modeled with a surface temperature of 7 °C.

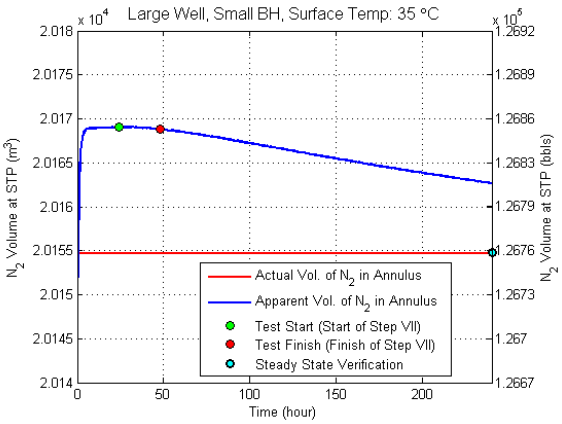

Figure 106 Actual and apparent volume calculations at STP for the Large well with Small uncased borehole modeled with a surface temperature of 35 °C.

F.2 Medium Well

The modeled actual and apparent volume results for the Medium well (through) modeled with three different uncased borehole (BH) sizes and two different brine surface temperatures are shown:

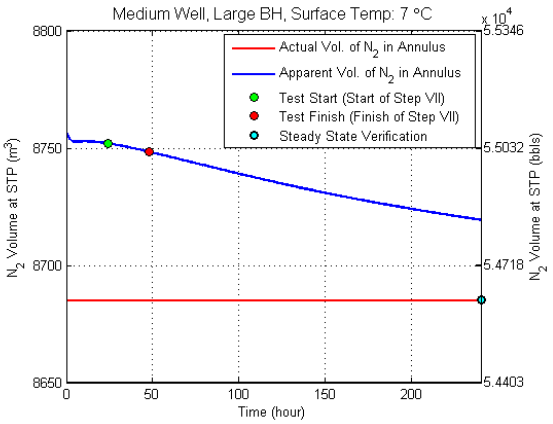

Figure 107 Actual and apparent volume calculations at STP for the Medium well with Large uncased borehole modeled with a surface temperature of 7 °C.

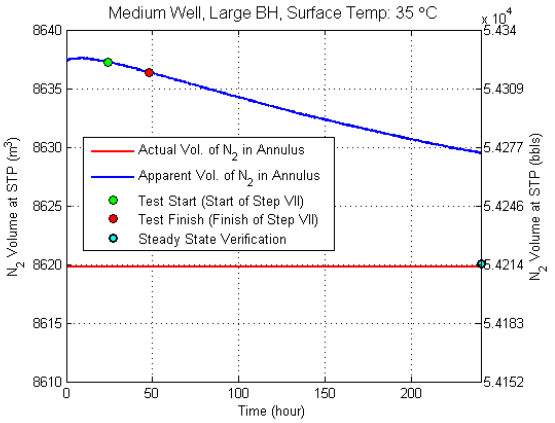

Figure 108 Actual and apparent volume calculations at STP for the Medium well with Large uncased borehole modeled with a surface temperature of 35 °C.

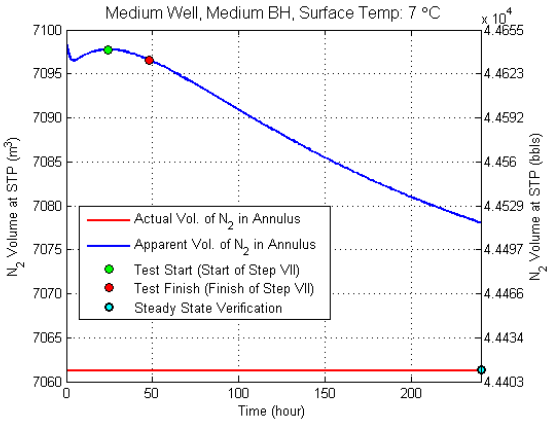

Figure 109 Actual and apparent volume calculations at STP for the Medium well with Medium uncased borehole modeled with a surface temperature of 7 °C.

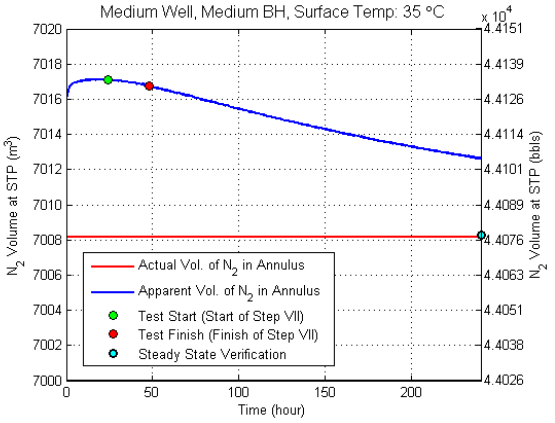

Figure 110 Actual and apparent volume calculations at STP for the Medium well with Medium uncased borehole modeled with a surface temperature of 35 °C.

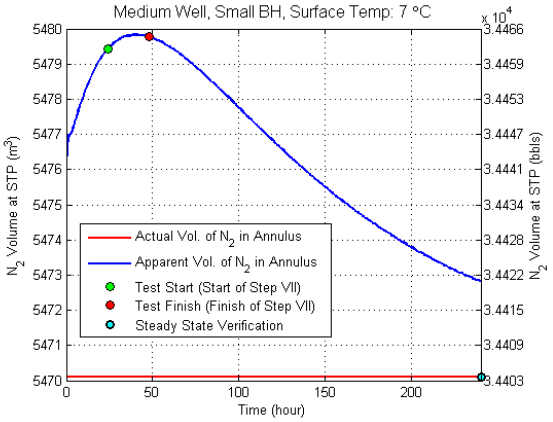

Figure 111 Actual and apparent volume calculations at STP for the Medium well with Small uncased borehole modeled with a surface temperature of 7 °C.

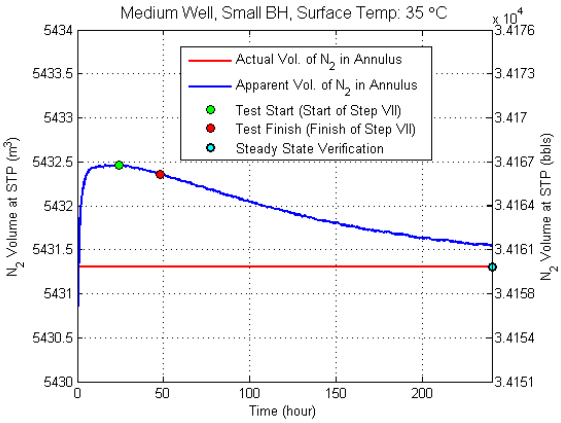

Figure 112 Actual and apparent volume calculations at STP for the Medium well with Small uncased borehole modeled with a surface temperature of 35 °C.

F.3 Small Well

The modeled actual and apparent volume results for the Small well (through) modeled with three different uncased borehole (BH) sizes and two different brine surface temperatures are shown:

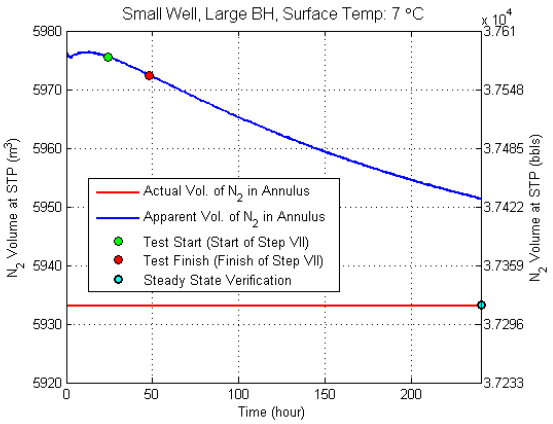

Figure 113 Actual and apparent volume calculations at STP for the Small well with Large uncased borehole modeled with a surface temperature of 7 °C.

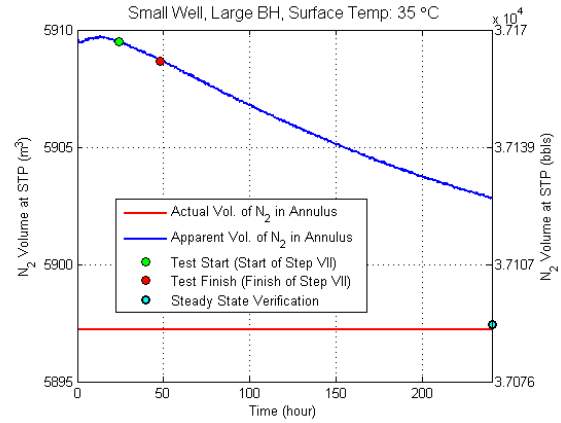

Figure 114 Actual and apparent volume calculations at STP for the Small well with Large uncased borehole modeled with a surface temperature of 35 °C.

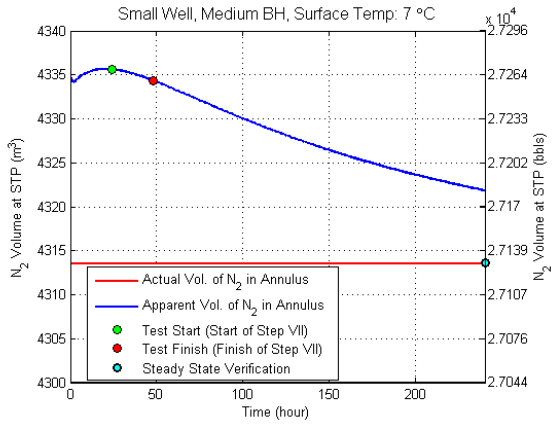

Figure 115 Actual and apparent volume calculations at STP for the Small well with Medium uncased borehole modeled with a surface temperature of 7 °C.

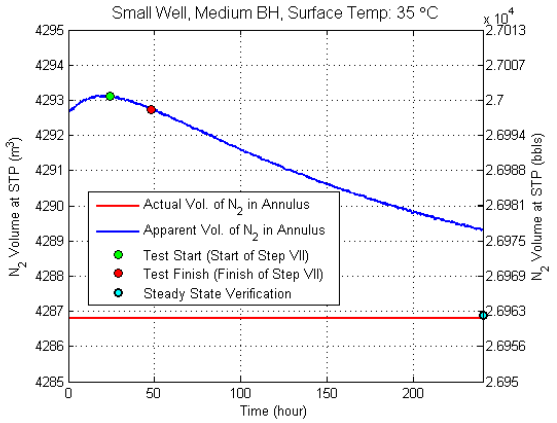

Figure 116 Actual and apparent volume calculations at STP for the Small well with Medium uncased borehole modeled with a surface temperature of 35 °C.

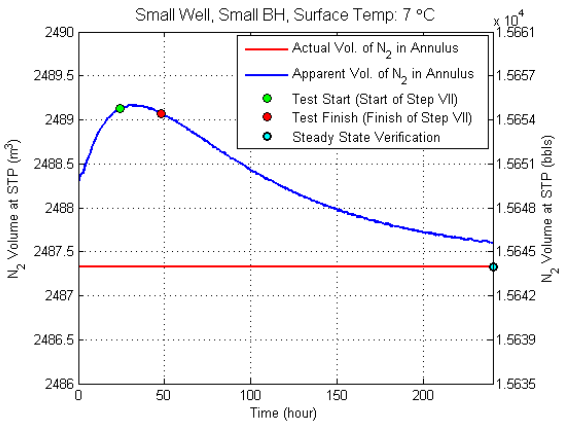

Figure 117 Actual and apparent volume calculations at STP for the Small well with Small uncased borehole modeled with a surface temperature of 7 °C.

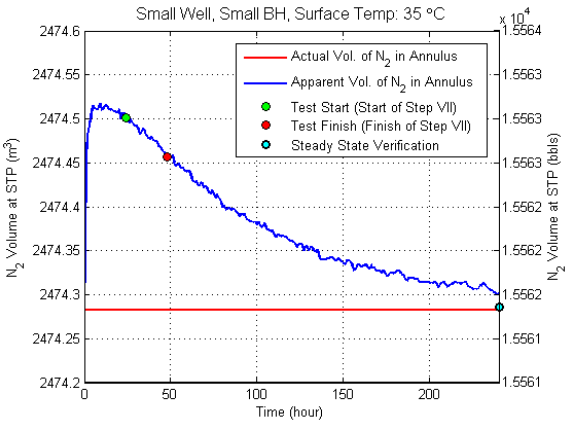

Figure 118 Actual and apparent volume calculations at STP for the Small well with Small uncased borehole modeled with a surface temperature of 35 °C.

Appendix G: Difference Between Annular and Injection String Temperature Distributions

The difference between the annular and injection string temperature distribution provides insight into the transient heat transfer phenomena that occurs during Steps VI and VII of a NBT. Instances where the annular temperature is almost uniformly greater than the injection string temperature also so a large initial jump in the sum of the difference between the annular and injection string difference and an increased initial apparent leak rate. Other common instances occur where the annular and injection string temperature difference is not uniform or of very small magnitude; these instances have an apparent leak rate that is relatively small or negative.

G.1 Large Well with Surface Temperature of 7 °C

The distribution of the temperature difference between the annulus and the injection string of the Large wells simulated with a surface temperature of 7 °C and the sum of the temperature difference with respect to time is illustrated by Figure 119 through Figure 124. The Large wells modeled with a 7 °C surface temperature all show a large initial increase in the value of apparent leak, this correlates well with the large initial increase in the sum of the temperature difference.

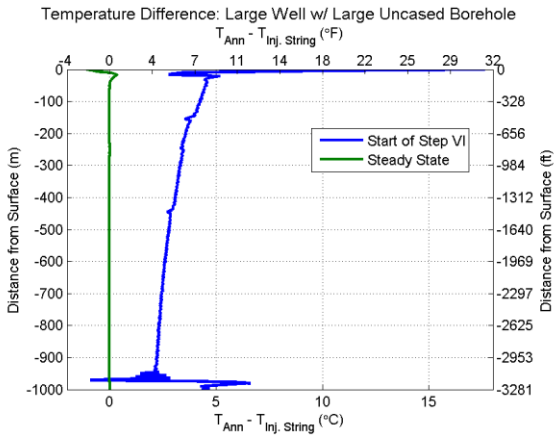

Figure 119 Temperature difference distribution of Large well with Large uncased borehole.

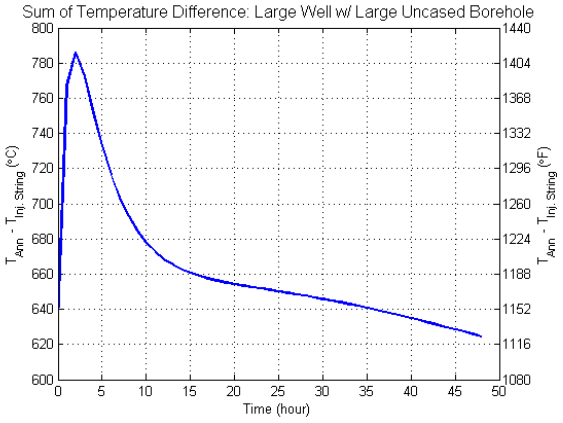

Figure 120 Sum of the temperature difference during Steps VI and VII of a Large well with Large uncased borehole.

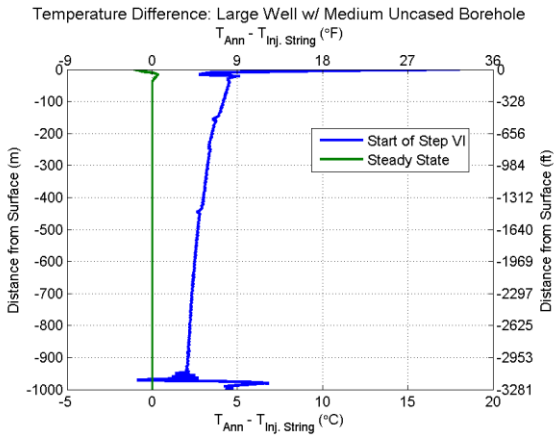

Figure 121 Temperature difference distribution of Large well with Medium uncased borehole.

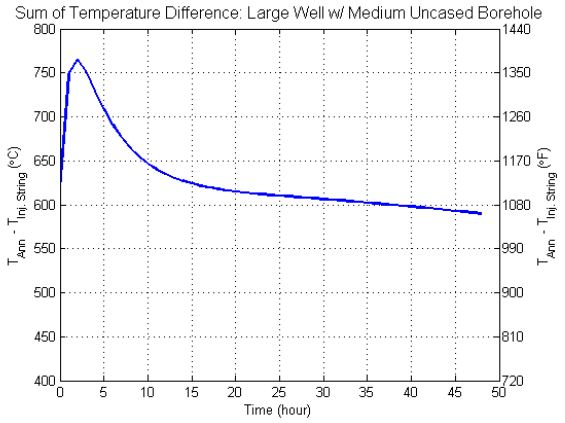

Figure 122 Sum of the temperature difference during Steps VI and VII of a Large well with Medium uncased borehole.

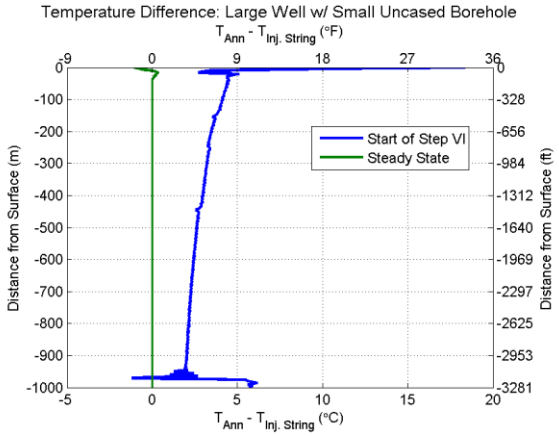

Figure 123 Temperature difference distribution of Large well with Small uncased borehole.

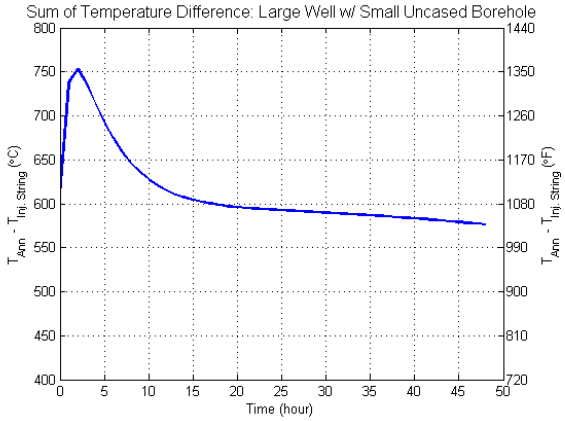

Figure 124 Sum of the temperature difference during Steps VI and VII of a Large well with Small uncased borehole.

G.2 Large Well with Surface Temperature of 35 °

The difference between the annular and injections string temperature profiles and the sum of the difference with time is shown for Large wells that were modeled having a surface temperature of 35 °C (Figure 125 through Figure 130).

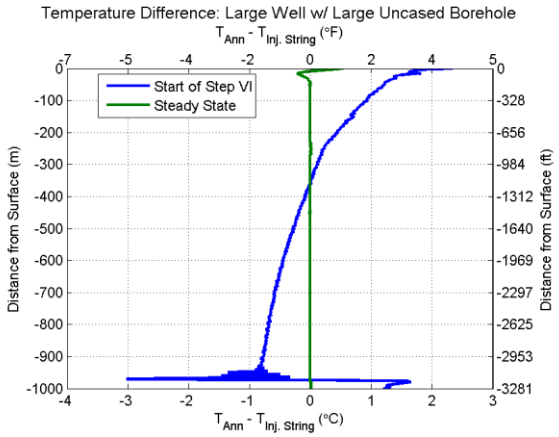

Figure 125 Temperature difference distribution of Large well with Large uncased borehole.

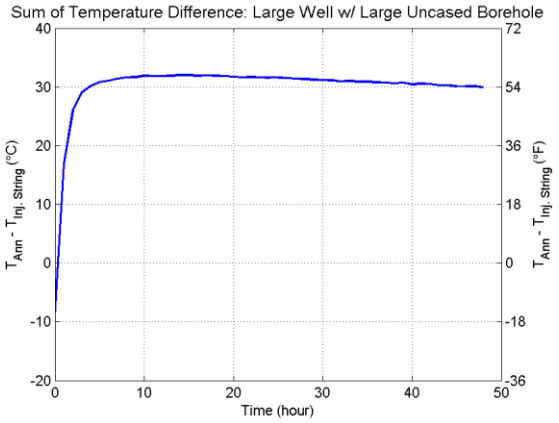

Figure 126 Sum of the temperature difference during Steps VI and VII of a Large well with Large uncased borehole.

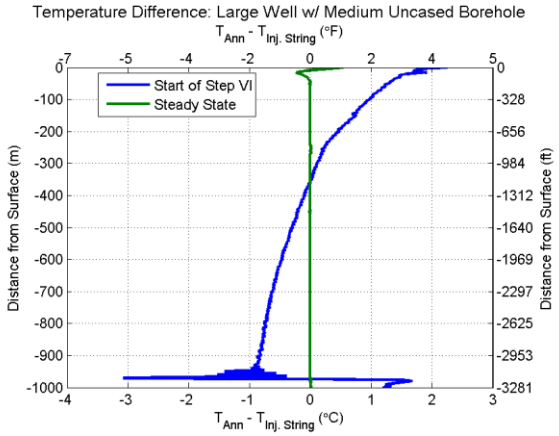

Figure 127 Temperature difference distribution of Large well with Medium uncased borehole.

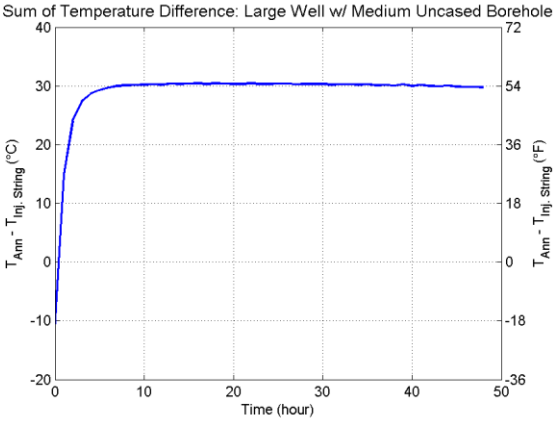

Figure 128 Sum of the temperature difference during Steps VI and VII of a Large well with Medium uncased borehole.

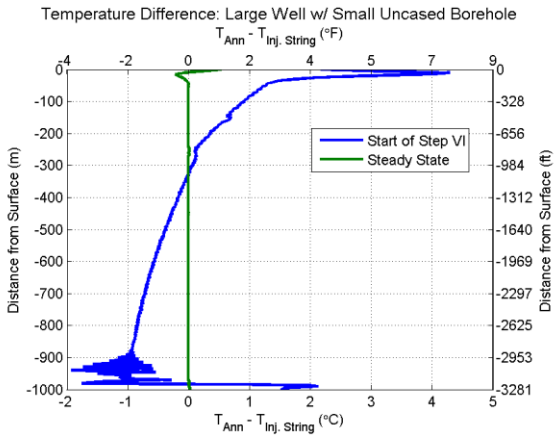

Figure 129 Temperature difference distribution of Large well with Small uncased borehole.

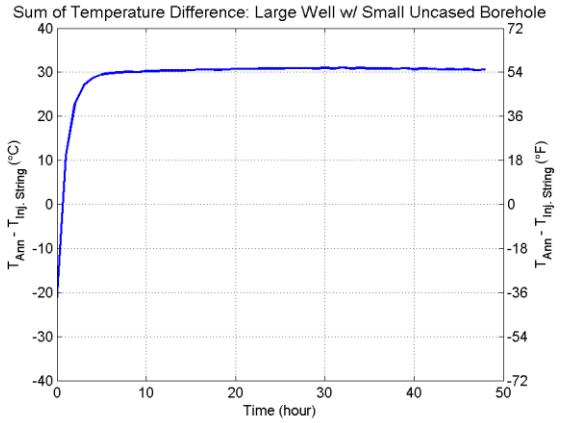

Figure 130 Sum of the temperature difference during Steps VI and VII of a Large well with Small uncased borehole.

G.3 Medium Well with Surface Temperature of 7 °C

The difference between the annular and injections string temperature profiles and the sum of the difference with time is shown for Medium wells that were modeled having a surface temperature of 7 °C (Figure 131 through Figure 136).

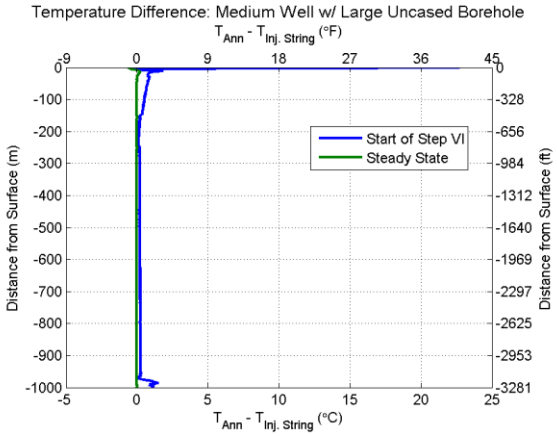

Figure 131 Temperature difference distribution of Medium well with Large uncased borehole.

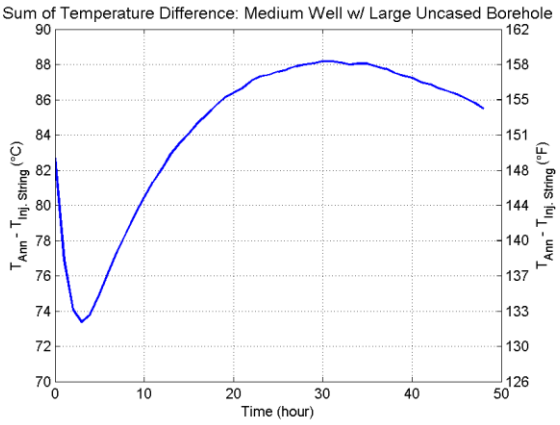

Figure 132 Sum of the temperature difference during Steps VI and VII of a Medium well with Large uncased borehole.

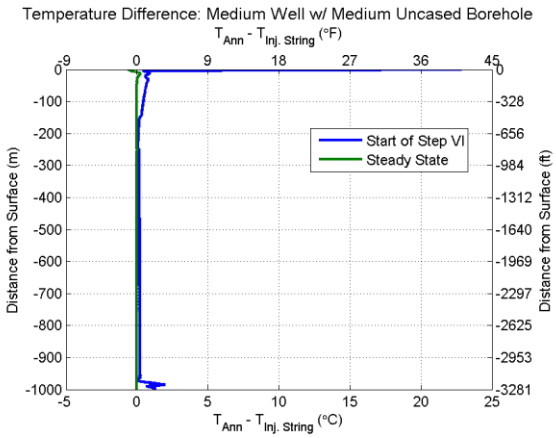

Figure 133 Temperature difference distribution of Medium well with Medium uncased borehole.

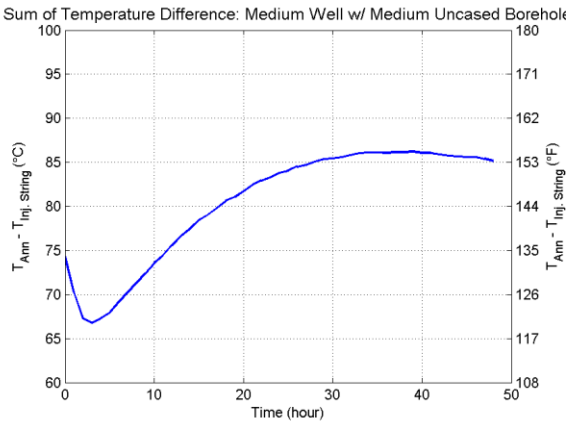

Figure 134 Sum of the temperature difference during Steps VI and VII of a Medium well with Medium uncased borehole.

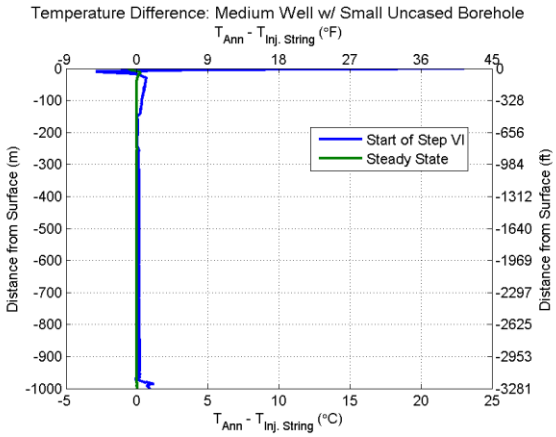

Figure 135 Temperature difference distribution of Medium well with Small uncased borehole.

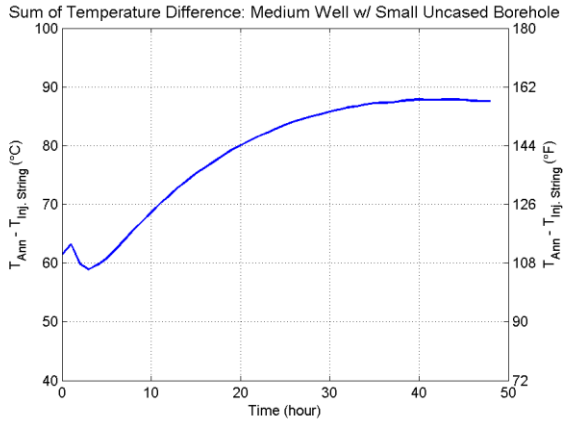

Figure 136 Sum of the temperature difference during Steps VI and VII of a Medium well with Small uncased borehole.

G.4 Medium Well with Surface Temperature of 35 °C

The difference between the annular and injections string temperature profiles and the sum of the difference with time is shown for Medium wells that were modeled having a surface temperature of 35 °C (Figure 137 through Figure 142).

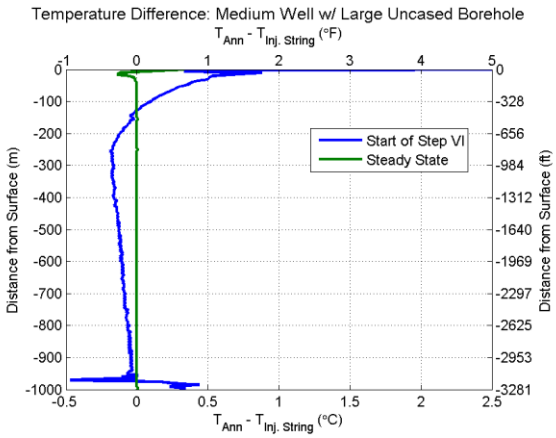

Figure 137 Temperature difference distribution of Medium well with Large uncased borehole.

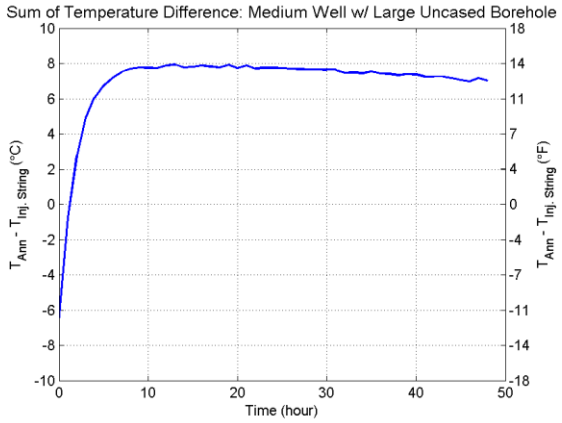

Figure 138 Sum of the temperature difference during Steps VI and VII of a Medium well with Large uncased borehole.

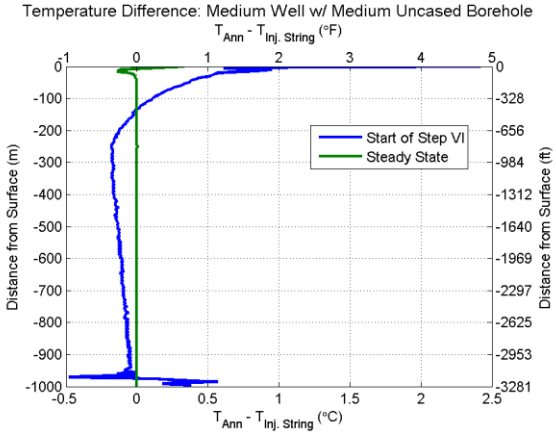

Figure 139 Temperature difference distribution of Medium well with Medium uncased borehole.

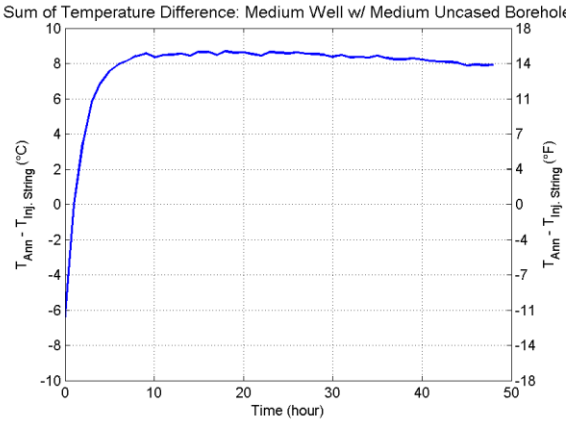

Figure 140 Sum of the temperature difference during Steps VI and VII of a Medium well with Medium uncased borehole.

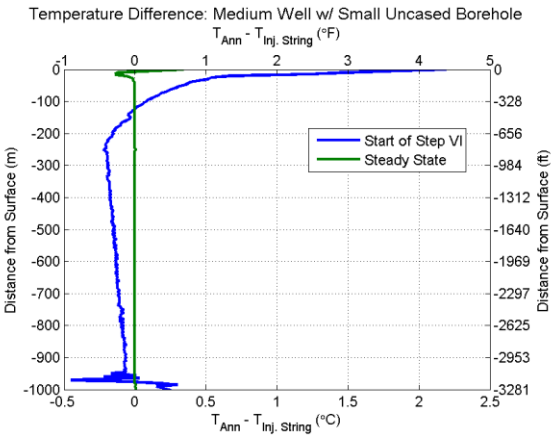

Figure 141 Temperature difference distribution of Medium well with Small uncased borehole.

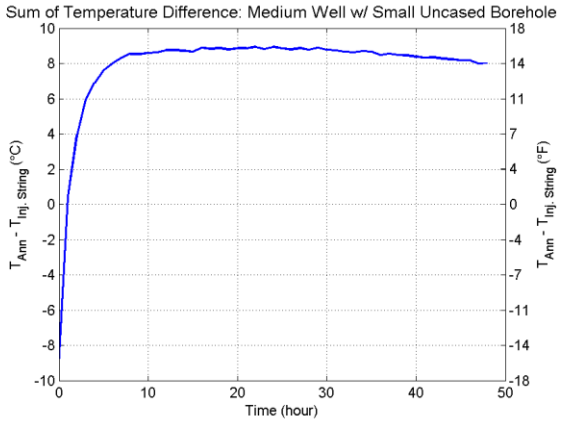

Figure 142 Sum of the temperature difference during Steps VI and VII of a Medium well with Small uncased borehole.

G.5 Small Well with Surface Temperature of 7 °C

The difference between the annular and injections string temperature profiles and the sum of the difference with time is shown for Large wells that were modeled having a surface temperature of 7 °C (Figure 143 through Figure 148).

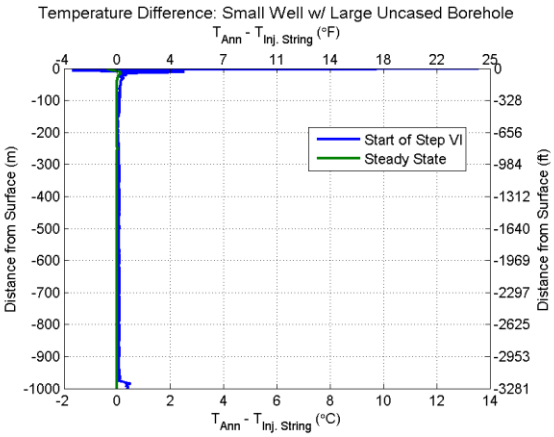

Figure 143 Temperature difference distribution of Small well with Large uncased borehole.

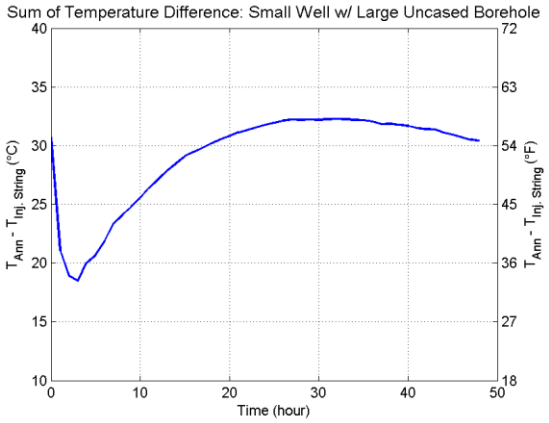

Figure 144 Sum of the temperature difference during Steps VI and VII of a Small well with Large uncased borehole.

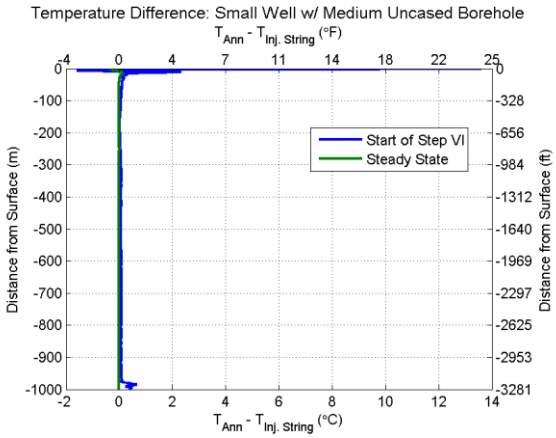

Figure 145 Temperature difference distribution of Small well with Medium uncased borehole.

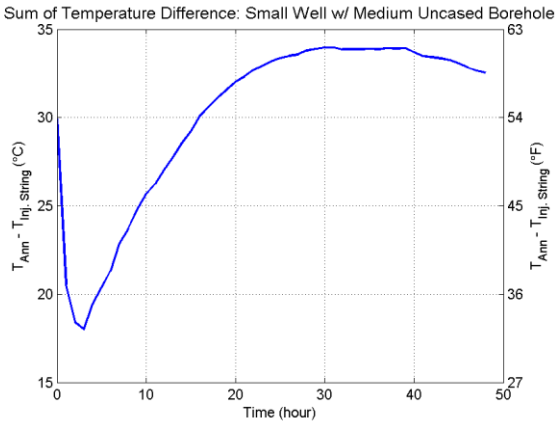

Figure 146 Sum of the temperature difference during Steps VI and VII of a Small well with Medium uncased borehole.

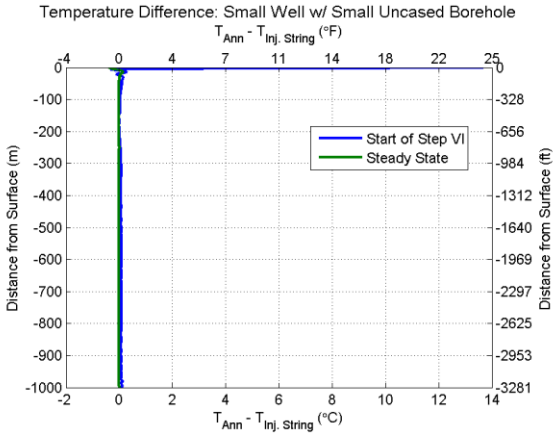

Figure 147 Temperature difference distribution of Small well with Small uncased borehole.

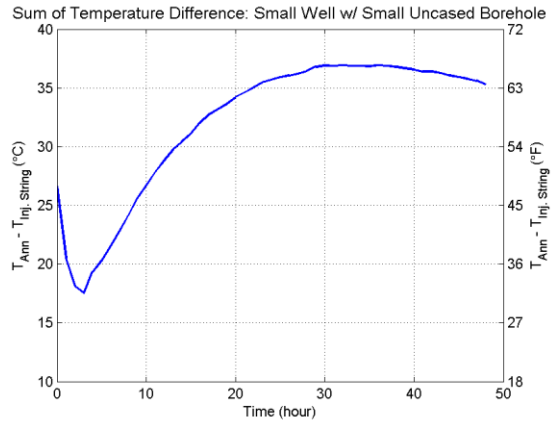

Figure 148 Sum of the temperature difference during Steps VI and VII of a Small well with Small uncased borehole.

G.6 Small Well with Surface Temperature of 35 °C

The difference between the annular and injections string temperature profiles and the sum of the difference with time is shown for Large wells that were modeled having a surface temperature of 35 °C (Figure 125 through Figure 130).

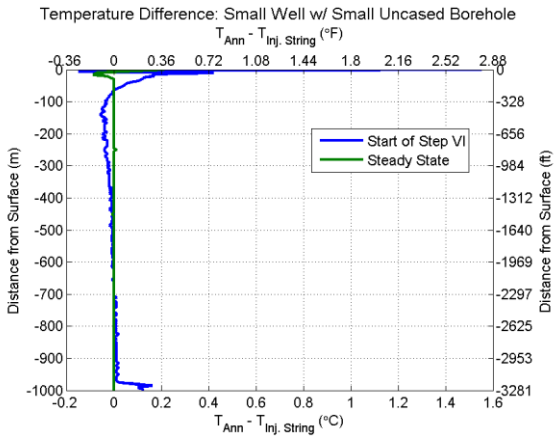

Figure 149 Temperature difference distribution of Small well with Large uncased borehole.

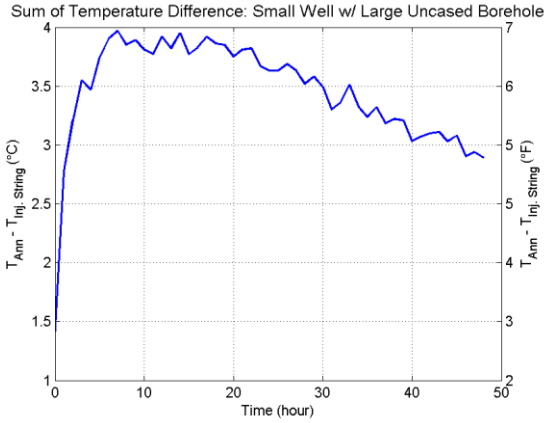

Figure 150 Sum of the temperature difference during Steps VI and VII of a Small well with Large uncased borehole.

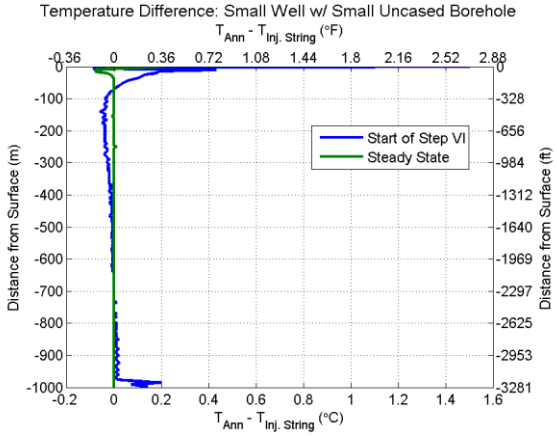

Figure 151 Temperature difference distribution of Small well with Medium uncased borehole.

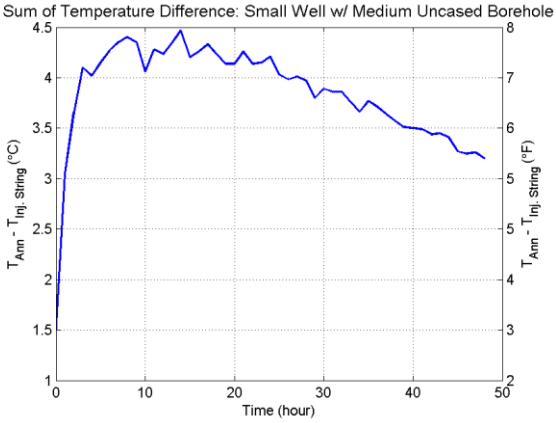

Figure 152 Sum of the temperature difference during Steps VI and VII of a Small well with Medium uncased borehole.

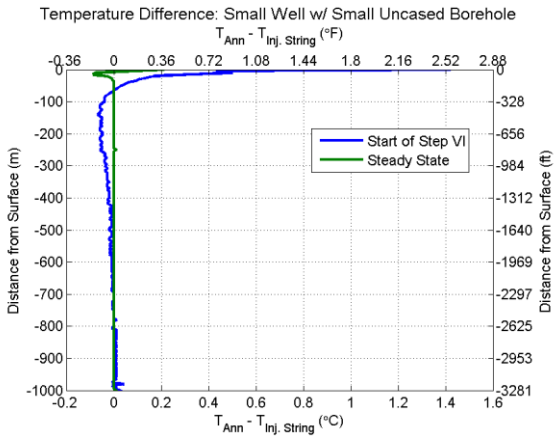

Figure 153 Temperature difference distribution of Small well with Small uncased borehole.

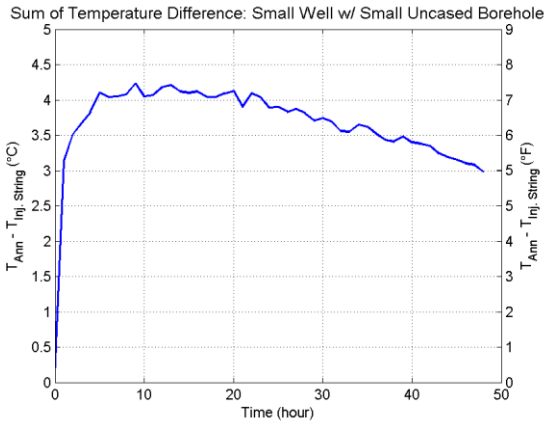

Figure 154 Sum of the temperature difference during Steps VI and VII of a Small well with Small uncased borehole.